SANDIA REPORT

SAND2014-17913

Unlimited Release

Printed October 2014

Large Motion High Cycle High Speed Optical Fibers for Space Based Applications

Peter G. Stromberg

Prepared by
Sandia National Laboratories
Albuquerque, New Mexico 87185 and Livermore, California 94550

Sandia National Laboratories is a multi-program laboratory managed and operated by Sandia Corporation, a wholly owned subsidiary of Lockheed Martin Corporation, for the U.S. Department of Energy's National Nuclear Security Administration under contract DE-AC04-94AL85000.

Approved for public release; further dissemination unlimited.

Issued by Sandia National Laboratories, operated for the United States Department of Energy by Sandia Corporation.

NOTICE: This report was prepared as an account of work sponsored by an agency of the United States Government. Neither the United States Government, nor any agency thereof, nor any of their employees, nor any of their contractors, subcontractors, or their employees, make any warranty, express or implied, or assume any legal liability or responsibility for the accuracy, completeness, or usefulness of any information, apparatus, product, or process disclosed, or represent that its use would not infringe privately owned rights. Reference herein to any specific commercial product, process, or service by trade name, trademark, manufacturer, or otherwise, does not necessarily constitute or imply its endorsement, recommendation, or favoring by the United States Government, any agency thereof, or any of their contractors or subcontractors. The views and opinions expressed herein do not necessarily state or reflect those of the United States Government, any agency thereof, or any of their contractors.

Printed in the United States of America. This report has been reproduced directly from the best available copy.

Available to DOE and DOE contractors from
U.S. Department of Energy
Office of Scientific and Technical Information
P.O. Box 62
Oak Ridge, TN 37831

Telephone: (865) 576-8401
Facsimile: (865) 576-5728
E-Mail: reports@osti.gov
Online ordering: http://www.osti.gov/home/reportform.html

Available to the public from
U.S. Department of Commerce
National Technical Information Service
5301 Shawnee Road
Alexandria, VA 22312

Telephone: (800) 553-6847
Facsimile: (703) 605-6900
E-Mail: orders@ntis.gov
Online order: http://www.ntis.gov/help/ordermethods.aspx#online

SAND2014-17913
Unlimited Release
Printed October 2014

Large Motion High Cycle High Speed Optical Fibers for Space Based Applications

Peter G. Stromberg
Advanced Flight Systems
Rajan Tandon
Cory Gibson
Materials Reliability
Benjamin Reedlunn
Solid Mechanics
Roger Rasberry
Garth Rohr
Organic Materials Science

Sandia National Laboratories
P.O. Box 5800
Albuquerque, New Mexico 87185-MS1244

Abstract

Future remote sensing applications will require higher resolution and therefore higher data rates (up to perhaps 100 gigabits per second) while achieving lower mass and cost. A current limitation to the design space is high speed high bandwidth data does not cross movable gimbals because of cabling issues. This requires the detectors to be off gimbal. The ability to get data across the gimbal would open up efficiencies in designs where the detectors and the electronics can be placed anywhere on the system. Fiber optic cables provide light weight high speed high bandwidth connections. Current options are limited to 20,000 cycles as opposed to the 1,000,000 cycles needed for future space based applications. To extend this to the million+ regime, requires a thorough understanding of the failure mechanisms and the materials, proper selection of materials (e.g., glass and jacket material) allowable geometry changes to the cable, radiation hardness, etc.

Acknowledgments

This work was funded under LDRD Project Number 165574 and titled *"Large Motion High Cycle High Speed Optical Fibers for Space Based Applications."*

Thanks to Kevin Brown, formerly Advanced Flight Systems organization and many others in Advance Flight Systems for helping pursue a broader approach to new missions space with an integrated view of Opto/Electrical/Mechanical design.

Table of Contents

Figures

Tables

Nomenclature

dB	decibel
DMA	Dynamic Mechanical Analysis
DOE	Department of Energy
DSC	Differential Scanning Calorimeters (temps/heat flow over thermal transitions)
EDS	Energy Dispersive X-Ray Spectroscopy
GIF	Gamma Irradiation Facility
GPa	Giga Pascal
HF	Hydrofluoric Acid
MPa	Mega Pascal
Mrad	Mega rad
nm	Nano Meter
N	Newton
N_2	Nitrogen Gas (Used for dry environments)
N/min	Newton/Minute ramp rate
Rad	Radiation exposure Rad Si (0.1 J/kg)
RH	Relative Humidity
SNL	Sandia National Laboratories
Tg	Glass Transition Temperature
TGA	Thermo gravimetric Analysis (weight change as a function of Temp/Atmospheric)
µm	micrometer

This page intentionally left blank.

1 INTRODUCTION

Future remote sensing applications will require higher resolution and therefore higher data rates (up to perhaps 100 gigabits per second) while achieving lower mass and cost. A current limitation to the design space is high speed high bandwidth data does not cross movable gimbals because of cabling issues. This requires the detectors to be off gimbal. The ability to get data across the gimbal would open up efficiencies in designs where the detectors and the electronics can be placed anywhere on the system. Fiber optic cables provide light weight high speed high bandwidth connections. Current options are limited to 20,000 cycles as opposed to the 1,000,000 cycles needed for future space based applications. To extend this to the million+ regime requires a thorough understanding of the failure mechanisms and the materials, proper selection of materials (e.g., glass and polymer coating materials), allowable geometry changes to the cable, radiation hardness, etc.

Consideration of the fiber for space flight will also require complete understanding of the reliability of the fiber optic cables throughout their life cycle. From procurement thru fabrication, storage and handling environments, launch and eventually space environments. One also needs to answer the questions on the life of fiber in a high relative humidity environment.

1.1 Mission Requirements

Fiber Optic cables for data transmission on space flight system will need to consider the full life cycle reliability for use in a critical flight application.[1] A chart of the various mission environments is shown below. Humidity is a very critical variable for fiber optics. A change from 10% to 50% RH will reduce the fiber strength in half. This reduction in strength happens almost instantaneously upon submersion in a higher RH, so careful handling of the fiber during the fabrication of a Satellite needs to be considered to maintain a reliable device. One needs to realize that the assembly process of a complicated Electro-Mechanical satellite system is usually completed at about 35% RH to keep the electrostatic discharge from occurring.

The most important driver for failure is stress in the fiber. This, of course, is driven by the bend radius. To truly design a reliable cross gimbal device we are evaluating the life at various bend radii. With a life estimate and a modeling understating of the applied stress we anticipate that we will predict life times and margins on whatever design we evaluate. Given these tools based on measured data for material reliability we can confidently design for many space flight applications.

[1] "Space Flight Qualification on a Multifiber Ribbon Cable and Array Connector Assembly", X. L. Jin, M. N. Ott, F. V. LaRocca, R. M. Baker, B. E.N. Keeler, P. R. Friedberg, R. F. Chuska, M. C. Malenab, S. L. Macmurphy, 2005, Vol 6308, Proceedings – SPIE The International Society for Optical Engineering.

Variable	Units	Min	Mid	High	Limit
Humidity (% RH)	% RH	0.8% RH	35% RH	50% RH	Submerged
Temperature Deg C	C	-40 C		+60 C	
Temp(Operation)	C	0		40C	
Radiation (K Rad Si lifetime)	K rad	100	5000	24000	
Radiation Rate	Rad/min	12 Rad/min		120 Rad/min	
Radiation + Tempature					
Bend radius (in)	In	0.25	0.5	1	1.5
Stress + Radiation (Bend)		0.25	0.5	1	1.5
Long term stress, humidity (mandrill)	mm/Mpa	1.8/2800	1.7/3000	1.45/3600	
Cycles		20k	200k	1000k	2000k
Measures					
Tensile Strength (Mpa)	Mpa	0	1300	2000	7000 Mpa
Transmission (db Loss)	db	0	2 db	4 db	

Table 1-1a: Mission Environments

1.2 Consideration of the Degradation Modes

We propose using advanced characterization and modeling tools to answer the fundamental question: Are there surface or interfacial cyclic fatigue mechanisms in optical fibers? Cyclic fatigue of fibers could jeopardize fiber reliability in remote sensing environments, either limiting design options (i.e., limiting to designs which enforce zero movement of the fibers) or reduced reliability/life in applications that require the fibers to move with a gimbaled payload. Emphasis is placed on fundamental understanding of the micro-mechanical origins of strength degradation in cyclic fatigue. One possibility is that fatigue strength is controlled by nm-sized surface pits formed by moisture reacting with the glass-surface. Such pits could "sharpen" in cyclic fatigue due to effects of wedged debris or asperity-contact. Another possibility is that the elastically mismatched core-clad interface delaminates during cyclic loading to cause fracture. Fundamental understanding of the degradation mechanisms and quantification of their effects will enable us to develop a model that can be used to specify safe-design limits for optical fibers.

2 MATERIALS

2.1 Materials Understanding

2.1.1 Technical Approach

It has long been known that slip irreversibility during cyclic loading produces crack growth in metals. However, strength degradation due to cyclic loading mechanisms in ceramics were only recognized in the late 1980's[2] While degradation in polycrystalline ceramics and composites is now understood to be caused by bridge degradation, phase transformations and interfacial sliding, cyclic effects for glasses are far less studied and understood. The reasons for this include the observation that the scatter in environmentally assisted crack growth (stress corrosion cracking in humidity[3]) can obscure the presence of mechanically induced fatigue crack growth ("true" cyclic fatigue). Furthermore, there is no widely accepted mechanism for cyclic fatigue in glass. Optical fibers, with their inherently high strength (>4 GPa), and extremely low strength variability (Weibull modulus, m>50, coefficient of variation of strength ~2-3%) provide an ideal materials platform to study the effects of cyclic fatigue. The high strength (and consequent small flaw size, <10 nm), implies that any fatigue process could lead to a drastic drop in strength. Determining the extent of cyclic degradation in rad-hard, space capable fibers is a key mission need.

Dill, et. al.[4] were the first to report a mechanically induced fatigue effect in bulk borosilicate glass at very slow (1.2nm/cycle) crack velocities. Oliver, et. al.[5] reported that cyclic loading drastically accelerates crack growth rates in hybrid glasses, even though the overall glass behavior was elastic. It was assumed that this was due to inelastic effects in the polymer. Matthewson et al.[6] tested telecom optical fibers, and found no effect of cyclic fatigue; however the cycles to failure were <5000. Ang et al.[7] plotted S-N curves for Bragg grating embedded on a fiber, and were able to identify the fatigue limit for their system. Fatigue was presumed to occur due to environmentally assisted crack growth.

Certain rad-hard fiber optics have a thin (~10 μm) fluorinated (F)-silica cladding, and a pure silica core (as opposed to a thick (~100 μm) pure silica clad, and a Ge-doped core for telecom fibers (used in Footnotes 6 and 7). Tandon et al.[8] have recently shown that the clad material has

---

[2] "Fatigue of Materials," S. Suresh, Cambridge University Press, 1998

[3] "Stress-corrosion mechanisms in silicate glasses," Matteo Ciccotti, J. Phys. D: Appl. Phys. 42 (2009)

[4] "Subcritical Crack-Growth Behavior of Borosilicate Glass under Cyclic Loads: Evidence of a Mechanical Fatigue Effect," S. J. Dill, S. J. Bennison and R. H. Dauskardt, J. Am. Ceram. Soc., 80 [3] 773–76 (1997)

[5] "Mechanical Fatigue of Hybrid Glasses," M. S. Oliver and R. H. Dauskardt, Small 2010, 6, No. 17, 1892–18967

[6] "Cyclic fatigue of high strength optical fibers in bending," M. J. Matthewson and V. Padiyar, SPIE Vol. 4215 (2001), pg. 53-59.

[7] "Tensile fatigue properties of fibre Bragg grating optical fibre sensors", J. Ang, H.C.H. Li, I. Herszberg, M.K. Bannister, A.P. Mouritz, International Journal of Fatigue 32 (2010) 762–768.

[8] "Elastic property differences in a multi-mode optical fiber and the effect on predicted mechanical lifetime," R. Tandon, T. E. Buchheit, and D. M. Berry, Journal of Non-Crystalline Solids, v 358, n 6-7, p 1009-1013, April 1, 2012

significantly lower elastic properties than silica. The response of this material to cyclic fatigue is unknown. Also, the F-silica and pure silica interface is close to the surface, and will be subjected to high tensile stresses in bending, leading to another possible degradation mechanism. A further complication is that fibers are coated with a ~70-µm polymer coating to minimize the introduction of surface flaws during handling. The durability of this coating to combined cyclic and rad environments is unknown. The delamination of the coating from the glass could potentially enhance fiber degradation (e.g., by allowing moisture ingress).

We will measure tensile and bending strength distributions of the fiber in inert and humid environments. The distribution of effective crack sizes can then be inferred from the strength data using a fracture mechanics analysis[9]. In this way a maximum possible flaw size can be identified (associated with cut-off strength in a 3-parameter Weibull distribution). A bending fixture, which will simulate the actual loading expected on the fiber in application, will be configured to test multiple fibers in cyclic fatigue in controlled humidity environments. Finite element analysis will allow the determination of stress distributions in the coated fiber. Fibers, with and without rad-exposures will be tested in cyclic fatigue at different stresses and for different numbers of cycles, and characterized using residual strength tests. Strength levels below the minimum strength determined from the fracture mechanics analysis will provide an indication of the effects of cyclic fatigue. The failure modes and degradation mechanisms will be elucidated using advanced characterization tools such as Atomic-force Microscopy, Scanning and transmission electron microscopy and nano-indentation. A limited number of (costly) tensile fatigue tests will be conducted in Year 2, to verify our models. These tests will subject meters of fibers to fatigue (as opposed to bending where ~10cm is tested). Combining the experimental results, and the understanding of degradation mechanism, S-N (stress-cycles to failure) curves will be generated. These curves will allow us to choose allowable design parameters for fibers in space application.

Using characterization and modeling tools, we will resolve the fundamental question of whether there is a surface or interfacial cyclic fatigue mechanism in high strength optical fibers, while creating tools for specifying safe-design tools for these space applications. The range of expertise needed, mechanical and physical characterization, numerical modeling and design, make this an appropriate challenge for a LDRD project at a national lab.

The GR-100/140-24HTA Nufern Specialty Multi-Mode Radiation Resistant Fibers (Figure 2-1) are designed for spacecraft and other applications in radiation environments. The core is surrounded by a cladding with a diameter of approximately 140 µm. A dual layer, high-temperature acrylate coating (52.5 um thick) protects the cladding at a diameter of 245 µm. The operating temperature is -55 to 125°C and the Prooftest Level is greater than or equal to 100 kpsi.

The dual layer acrylate is a proprietary Nufern coating, so we were unable to obtain bulk coating material for our qualification testing; however, Nufern did share with us the technical data sheets for referencing and comparison purposes. The layer that immediately surrounds the cladding is

[9] "Predicting Fracture in Micron-Scale Polycrystalline Silicon MEMS Structures," E. D. Reedy, Jr., B. L. Boyce, J. W. Foulk III, R. V. Field, Jr., M. P. de Boer, and S. S. Hazra, J. Microelectromech. Syst., 20 (2011), pp. 922-932.

referred to as the Primary and has a Tg near -20°C, so it is rubbery at room temperature. The Secondary surrounds the Primary and has a Tg close to 90°C, so it is glassy at room temperature. Typical polymers such as these behave as an elastic solid at low strains following Hooke's Law where Young's modulus is determined by the slope of the stress-strain curve. At some point, the slope of the stress-strain curve begins to shift from linearity such that there is no longer an increase in stress with increasing strain. This is called the yield point of the polymer. Yield strength is calculated by dividing the force at the yield point by the cross-sectional area of the sample.

Young's modulus is an intrinsic property often referred to as the stiffness of the material. According to the data sheet provided by Nufern, at room temperature the modulus of the dual layer acrylate coating is dominated by the Secondary at just above 500 MPa. To qualify this and to obtain modelling data, stress-strain curves were generated for the dual layer acrylate from pristine fibers obtained from Nufern. This was accomplished by removing the coating from the cladding and then loading it into a dynamic mechanical analyzer (DMA) where it was pulled apart at a defined rate. Intrinsic properties, such as the glass transition temperature (Tg) and thermal decomposition, were also measured using differential scanning calorimetry (DSC) and thermogravimetric analysis respectively (TGA). Ultimately, this approach allowed us to answer the questions of whether: (a) the polymer coating might degrade and the cracked coating could induce failure of the glass fiber; and (b) the coating protects the glass but has a permeable diffusion barrier that could cause problems in humid environments.

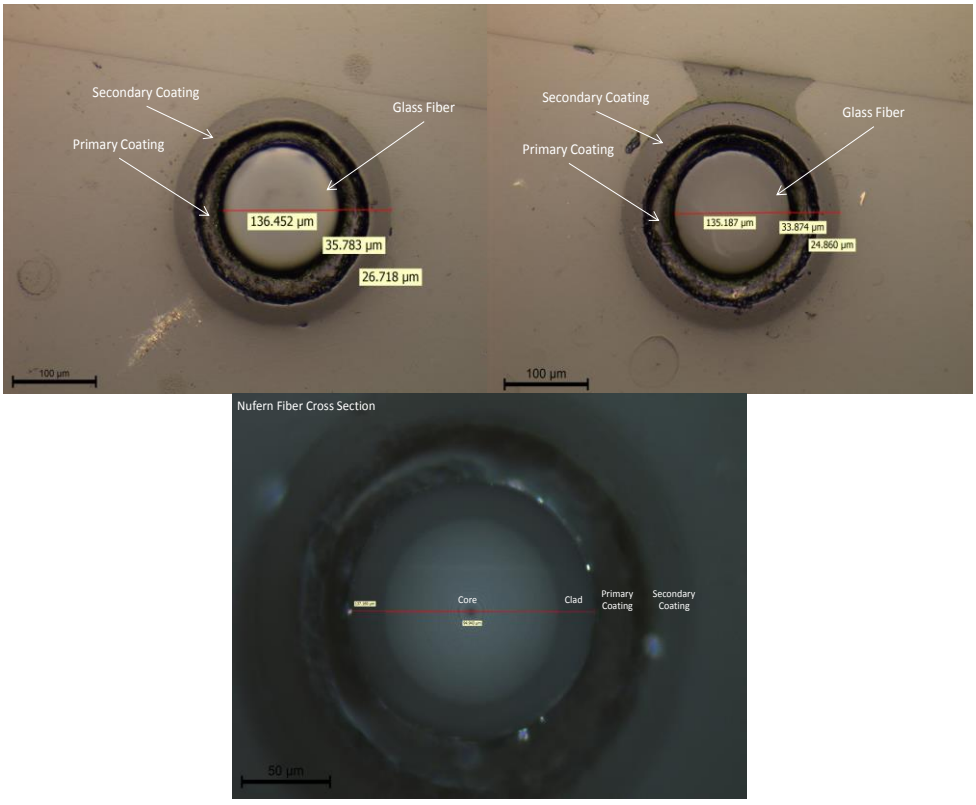

Figure 2-1. Nufern Fiber Cross-section with labels.

As a confirmation of the optical materials and doping, we also performed an Energy-Dispersive X-ray spectroscopy (EDS) to see the dopant and location, results are shown in Figure 2-2.

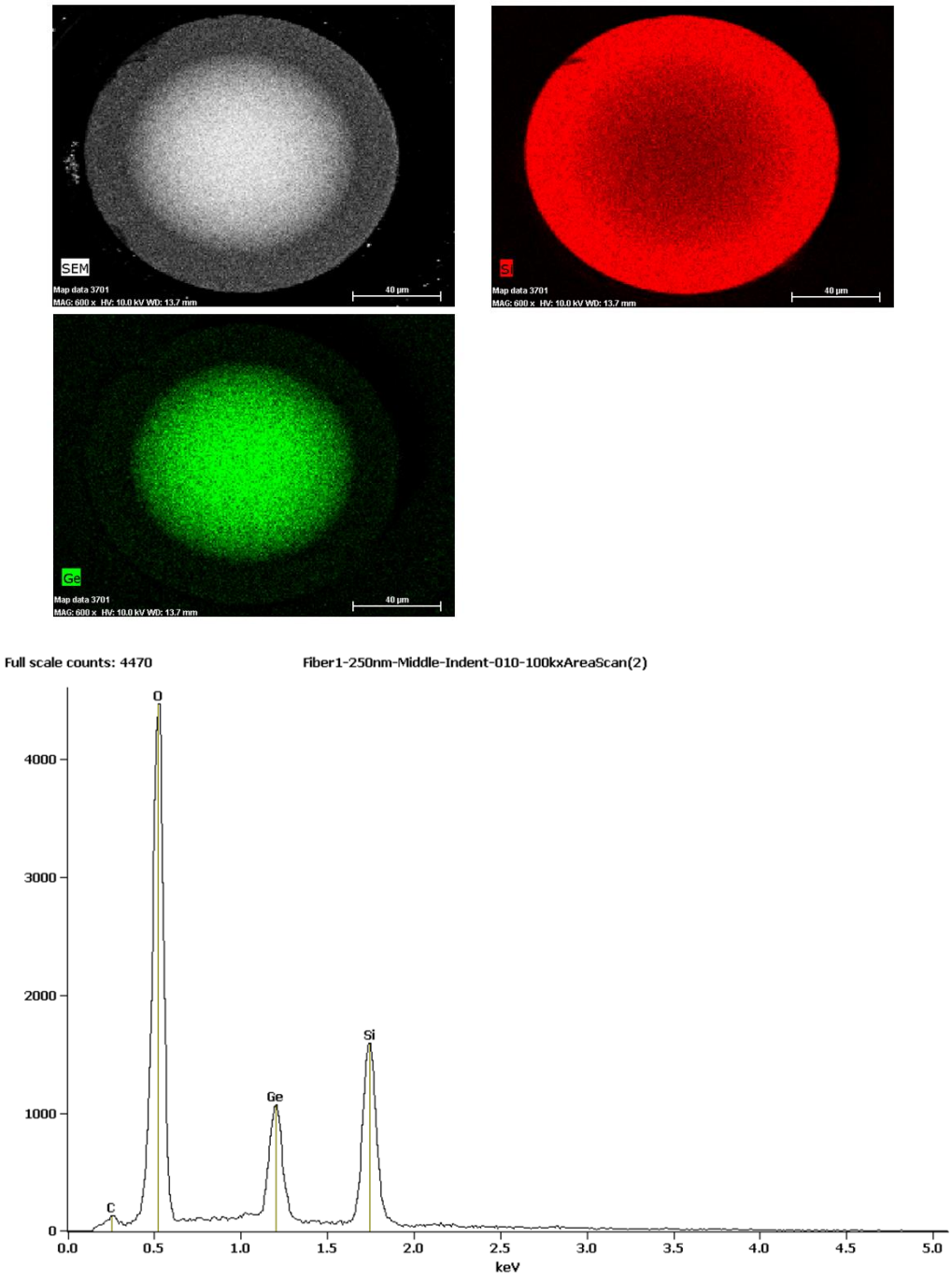

Figure 2-2. Nufern Fiber-EDS Spectra showing Si (Red) and Ge (Green)

2.2 Materials Testing

Our first attempt to characterize the thermomechanical properties of the polymer coating was unsuccessful. This was carried out by stripping the polymer coating away from the fiber using a Micro-Strip tool (0.006" hole) and then analyzing the shavings using TGA and DSC. Though complete thermal decomposition occurred up to 500°C, no Tg was observed in the DSC plot. The same result was achieved by running a large quantity of pristine fiber (coating intact).

Our next effort was successful as we were able to remove the coating by simply soaking the fiber in a hot water bath at 71°C for several days. During this time, the polymer began to swell and the water wicking effect led to delamination at the polymer-glass interface. Approximately 1" long pieces of the tubular coating were removed using the Micro-Strip tool and the coatings dried in an oven overnight at 50°C to remove the water. The storage modulus was measured using DMA via multi-frequency – strain over a temperature range of -50 to 150°C with a ramp rate of 3°C per minute under nitrogen. Stress-strain curves were generated at room temperature under force control conditions (3.0 N/min to 18.0 N) under a nitrogen atmosphere (Figure 2-3).

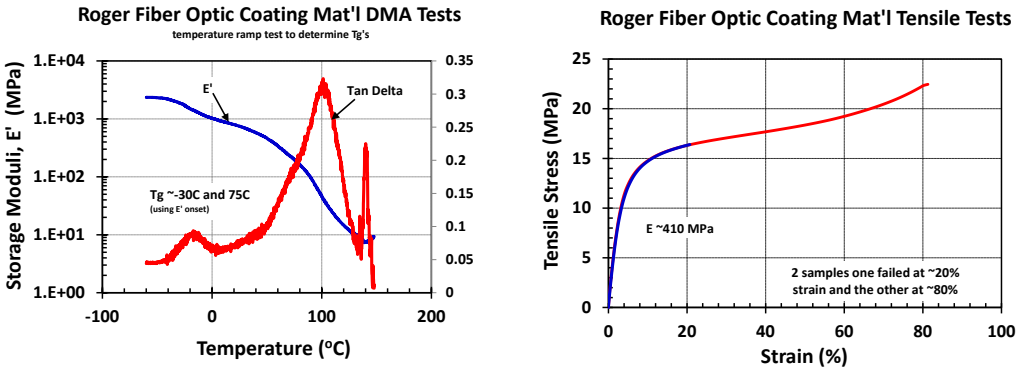

Figure 2-3. Thermomechanical data for polymer coating obtained via water wicking method.

Two distinct Tg's were observed with onsets of -30 C and 75°C. This data is consistent with the Spec sheet provided by Nufern corresponding to the primary and secondary coating respectively. Young's moduli were obtained from the slope of the stress-strain curve prior to the yield point. The values for two samples were around 410 MPa, which is consistent with Nufern. Most of the contribution comes from the secondary coating, which is glassy at room temperature whereas the primary coating is rubbery. To confirm this, the sample was analyzed at -40°C and stress-strain curves generated in a similar manner to the previous ones (force control, N_2, 0.25 N/min to 3.0 N). As shown in Figure 2-4, the Young's modulus was a factor of 2 higher (1170 MPa) relative to the modulus at room temp which is explained by higher modulus of the primary coating that is glassy at this temperature.

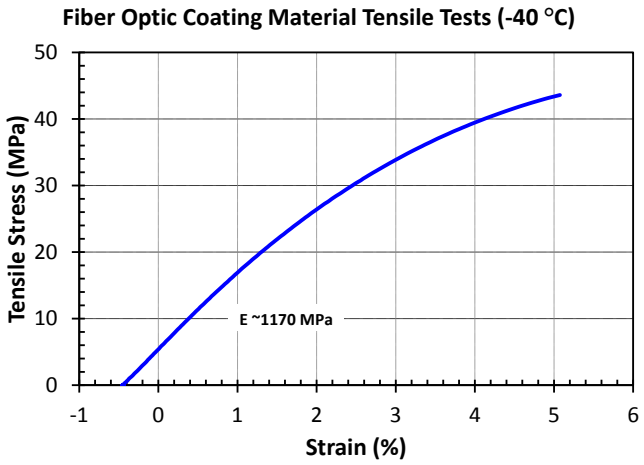

Figure 2-4. Stress-strain curve at -40°C for polymer coating obtained via water wicking method.

At room temp, it was somewhat difficult to elucidate the yield point but nominally it was thought to be above 12 MPa (Figure 2-5). If the sample had yielded below this value, then the modulus would be different on subsequent cycling of the sample. This was demonstrated from a sample that was cycled 3 times at room temperature (Figure 2-5). The conditions were: Force control, N_2, ramp stress = 2 Mpa/min to 12 ramp 2 MPa/min to 0, repeat segment 2 times, room temp. The modulus increased slightly during thermal cycling but overall did not change significantly.

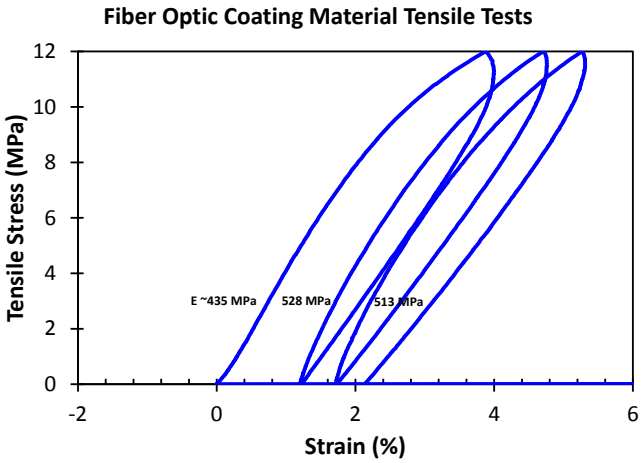

Figure 2-5. Stress-strain curve (room temp) for polymer coating cycled three times.

The next step was to look at load to failure at room temperature. This was done under force control conditions, N_2, and a ramp force rate of 0.25 N/min to 5.0 N. The sample failed around 20% strain. As illustrated in Figure 2-6, there is variation in the modulus depending on where the slope is measured.

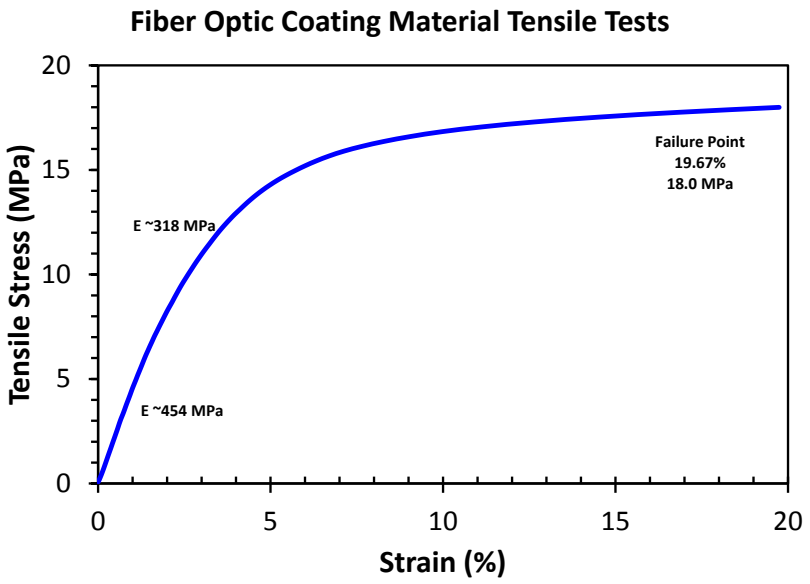

Figure 2-6. Stress-strain curve (room temp) for polymer coating to failure.

Up to this point, the polymer was obtained by soaking the fiber in a hot water bath. The polymer swells and water wicks at the interface leading to delamination so it is easily removed using a Micro-strip tool. To ensure that the polymer was not being perturbed during removal, we investigated whether it was possible to use HF to etch the glass without damaging the polyacrylate. Here, the fiber was cut into approximately 1" sections and 2-3 pieces were then immersed in 49% HF for 24 hours. This ample amount of time allowed for the glass core/cladding to be completely etched by the HF leaving behind hollow polymer tubes. The tubes were then rinsed with a copious amount of deionized water and placed on a hot plate at 110°C for 10 minutes to drive off the water. Visual and mechanical evidence was confirmed via optical microscope with the primary and secondary coating thicknesses being virtually identical to the pristine fiber (Figure 2-7) and the modulus at room temperature (Figure 2-8) was in excellent agreement with that obtained via the water wicking method.

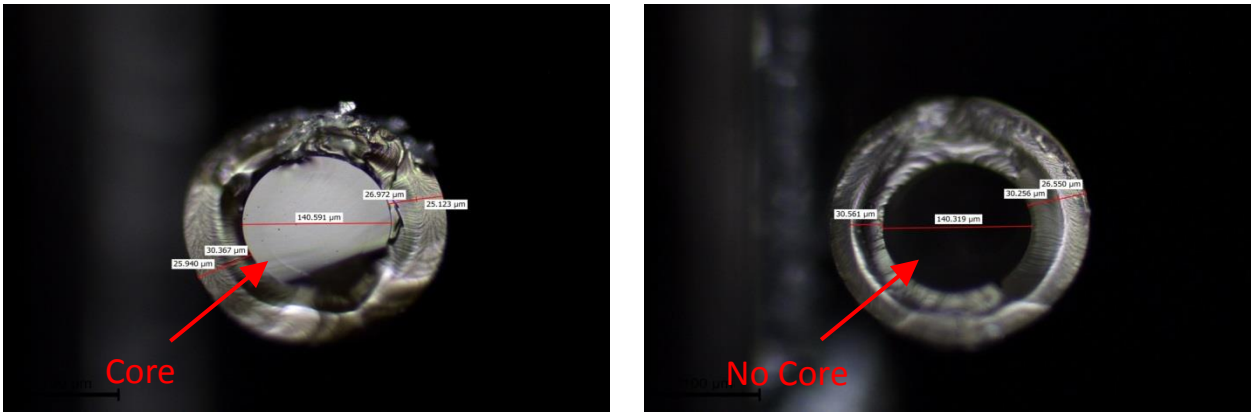

Figure 2-7. Optical micrographs of the as received fiber (left) and post HF etch fiber (right).

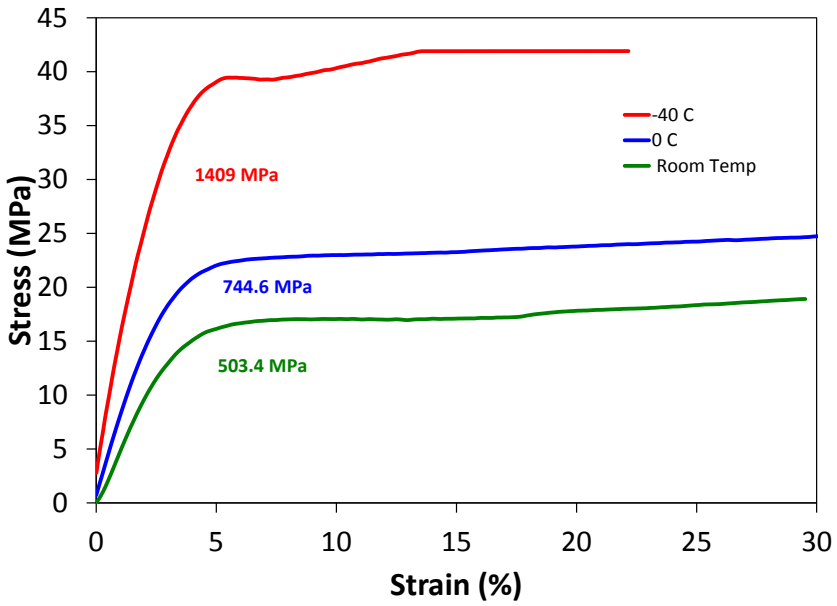

Figure 2-8. Stress-strain curves at different temperatures for the control etched with HF.

Next, fibers were exposed to radiation at 0.1, 5, and 24 Mrad total dosages. The fibers were etched using HF procedure and then analyzed under controlled force conditions with a ramp force rate of 0.25 N/min to 5.0 N at room temp under an inert atmosphere. The modulus increased marginally with dosage and a slight yellowing of the coating was observed as well (Figure 2-9).

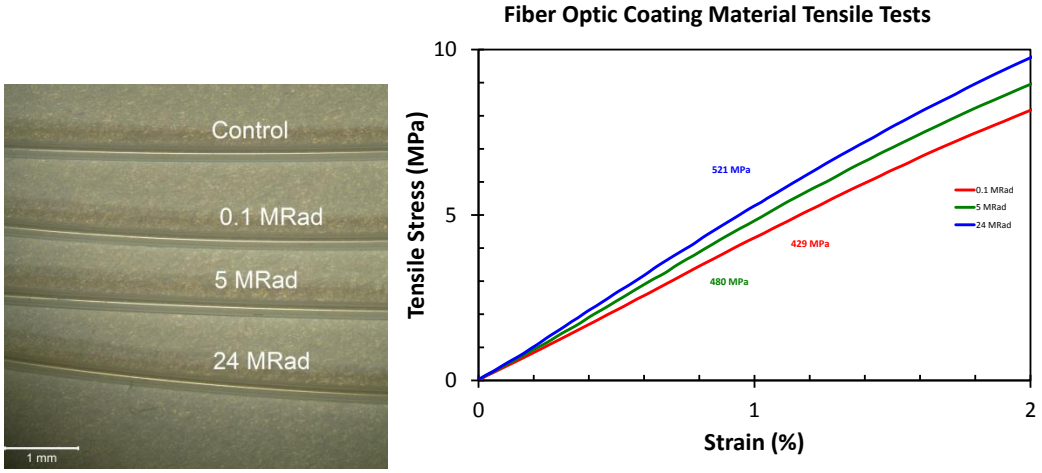

Figure 2-9. Optical micrographs of the rad exposed fiber (left) and stress-strain curves (right).

Around this time, a question was posed as to whether the sample was slipping in the grips of the DMA and an accurate measurement was being taken. Theoretically, the sample would fail at the grips because that is where the stress is localized. To ensure that slippage was not occurring, a 5 Mrad sample that had been etched was run under force control both in the presence and

absence of sandpaper. As seen in Figure 2-10, the sample failed near the grips in both cases and there was little variance in the modulus.

Figure 2-10. Rad exposed fiber modulus measured with and without sandpaper grip.

Next, we discovered that it was important to hold strain rate constant because it was easier to calibrate most constitutive models for polymers where the data is at a constant strain rate. As such, we switched to measuring the modulus via strain control (aka displacement control). Rather than destroy one of the samples, a commercial 2 µm thick Mylar film was run on DMA in both the strain control and stress control modes. As you can see in Figure 2-11, there was very little difference between these runs. The spec sheet for this MYLAR C material lists the tensile strength (stress) as 151.7MPa and both of the samples failed near this value. Though the noise was slightly higher in the strain control mode, the data were in good agreement overall.

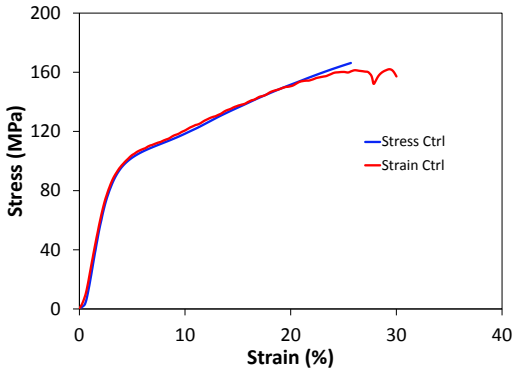

Figure 2-11. Stress-strain curves for Mylar C measured via strain control and stress control modes.

Finally, a comprehensive evaluation of each fiber was conducted using DMA and pictures taken for when the dual acrylate coating broke (Figure 2-12 and Figure 2-13). Each sample was etched via the HF method and run under strain control conditions without using sandpaper. The sample was first equilibrated at -40, 0, rt, or 60°C under N_2 and then run under ramp displacement at 500 µm/min to 15,000 µm. Overall, the moduli collectively decreased as the measuring temperature increased and values for the rad exposed fibers were only marginally different from the control. These results suggest that the dual acrylate coating on the GR-100/140-24HTA

Nufern Specialty Multi-Mode Fibers is radiation resistant which is necessary for space applications.

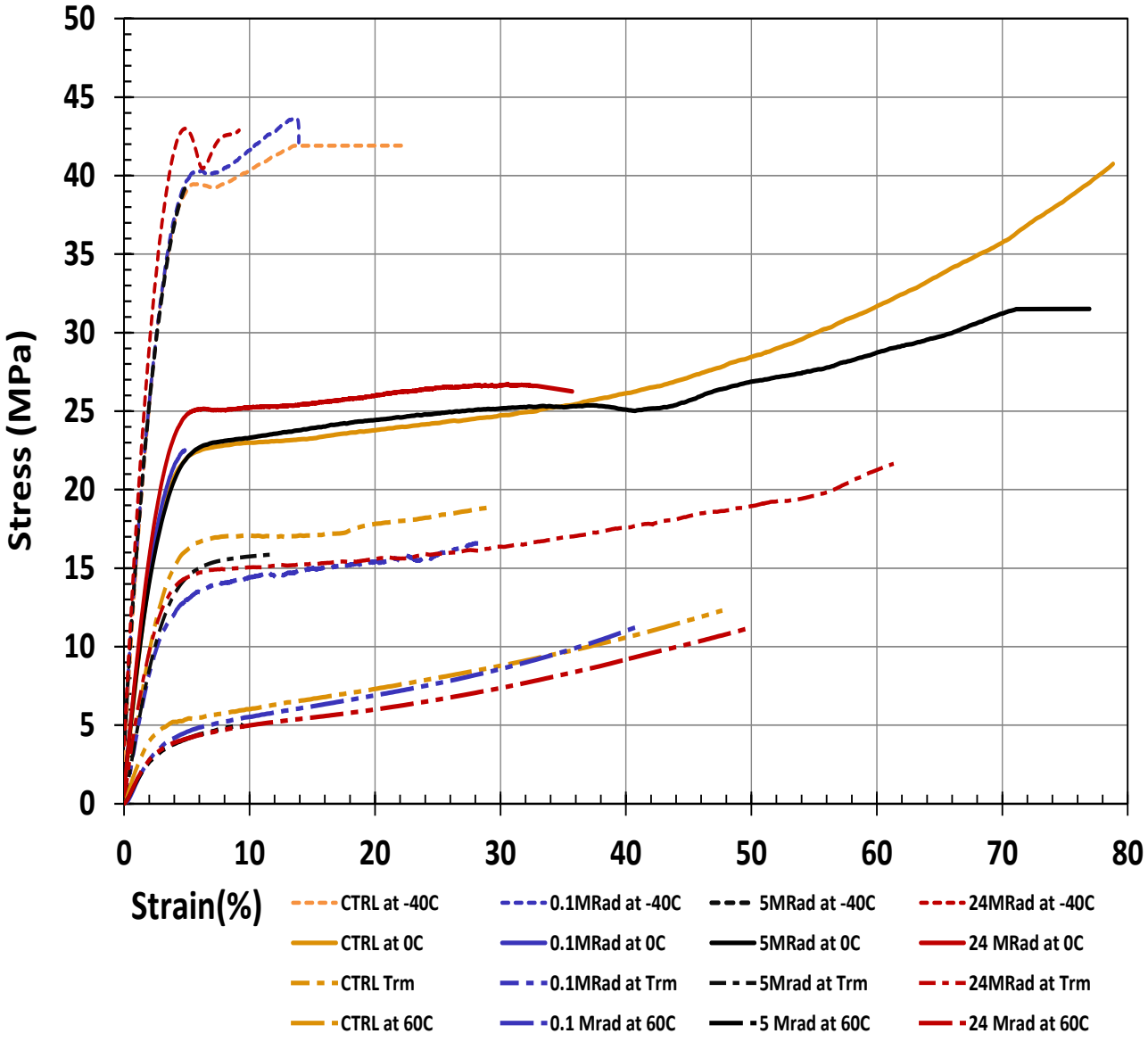

Figure 2-12. Radiation Effects on Dual Acrylate Coating Moduli

Figure 2-13. Stress-strain curves and images for control, 0.1, 5, and 24 Mrad exposed polymer.

2.2.1 Strength Quantification

A two-point bend testing set up was used to quantify the strength of the fibers, at different humidity levels, after various radiation exposure treatments, and to generate strength degradation data as a function of time under load in humid environments. The two-point bend test set up is shown schematically in Figure 2-14. The test involves constraining a bent loop of fiber between two faceplates which are then brought together until the fiber breaks. The fiber is held inside grooves in the faceplate. The faceplates are brought together by a computer-controlled stepper motor that is halted when the fiber fracture is sensed by an acoustic detector. The failure strain is then calculated from the guide plate separation at fracture and the fiber diameter. This type of testing has several advantages over tensile testing of fibers as enumerated by Matthewson, et. al. (1986):

- There are no gripping problems. Fibers with a compliant coating (e.g., silicone) or a degraded (e.g., by heat or water) higher modulus coating cannot easily be gripped in tension. Fibers, whether coated or uncoated, can readily be broken in bending. Although

the accuracy of the results may be questionable in some of these cases, comparative assessments can be made.

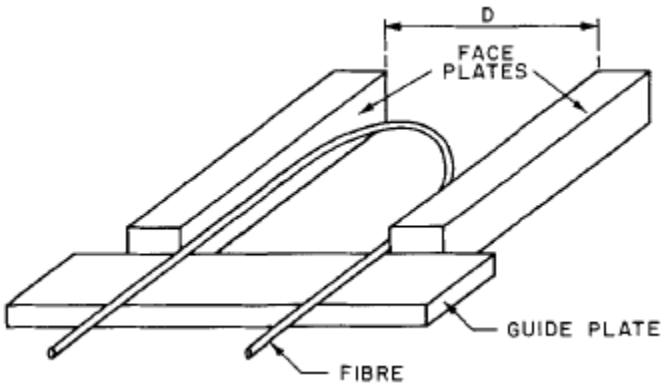

Figure 2-14. Schematic of the two-point bend setup for testing fiber strength.

- Only a small length of fiber is subjected to stress; therefore, it is easy to "zero in" on a region of interest if it is small.
- The bending technique is readily made highly accurate (in a relative sense, see below for absolute accuracy); it is easier to accurately measure the separation of the faceplates than the analogue output of a load cell. The faceplate separation at fracture is typically =2000 μm for a high-strength fiber and the accuracy to which this is determined is the step length of the stepper motor. A motor with a small step size could be used for higher accuracy but the maximum achievable loading rate (faceplate velocity) is proportionately lower. The system is easily computerized, the components are readily available and inexpensive, and the apparatus is compact and simple to use.
- The fiber can easily be immersed in an environment. Liquid-nitrogen strengths have been found with comparative ease. Alternatively a gaseous or liquid environment can be blown or dripped on the small section of fiber under test, obviating the need for an environmental chamber.
- Since only a small length of fiber is under a high stress, only a small length of fiber disintegrates into dust at fracture. The fiber diameter close to the fracture can then be measured.
- Only a small length of fiber (~6-8 cm) is used. This is clearly an advantage if only small quantities of fiber are available.

However, there are some problems with the bending technique:

- Absolute accuracy is not as good as in tension since it is difficult to accurately determine the position of zero separation of the faceplates. Also, the overall fiber diameter is subtracted from the faceplate separation before calculation of the fracture strength and this can lead to significant errors for coated fibers since the coating thickness and concentricity can be variable, but more importantly, the coating can deform under the contact stresses thus reducing the effective fiber diameter. As noted, comparative assessments can still be made.

- For strong fibers (strain to failure> 1%) the linear elastic analysis for the bend geometry becomes inaccurate since it assumes small strains. However, the results are still qualitatively correct, though quantitatively the error in the predictions increases with increasing strain (i.e., strength).The tested length of fiber in bend is very small and therefore bending results are not useful for inferring the strength statistics of kilometer lengths of fiber.
- The mean strength of a material depends on the specimen size because of the stochastic nature of the distributions in position and size of strength-reducing defects; the larger the specimen, the greater the probability of finding a larger defect. In tension, tested length is pre-determined; however, this is not the case for bending as the length of bent fiber depends on the radius of curvature at fracture and hence on the strength. Also, the strength depends on the tested length, which itself depends on the strength!

The two-point bend testing setup used in this work was purchased from Fiber Sigma Inc., NJ, and Figure 2-14 is an image of test set up used in this study. The stepper motor, moveable jaws to bend the fiber, and the acoustic sensors and other hardware are enclosed in a polymer box that can be sealed. This allows the humidity in the box to be controlled from very dry (~0% RH) to ~95% RH. Changing the rate of the stepper motor motion allows for different stressing rates to be applied to the fiber. The jaws used have multiple grooves allowing the placement and testing of multiple fibers. However, it was often observed that the failure of one fiber triggered failures of the others, possible due to impact of the snapped fiber with the still intact ones. The multiple fiber capability was most helpful while conducting initial cyclic fatigue tests: 10 fibers at a time could be loaded and cyclically loaded for a large number of cycles before failure. They could then be tested to failure (after the prescribed number of cyclic tests) to see if the applied loading has caused any degradation in strength.

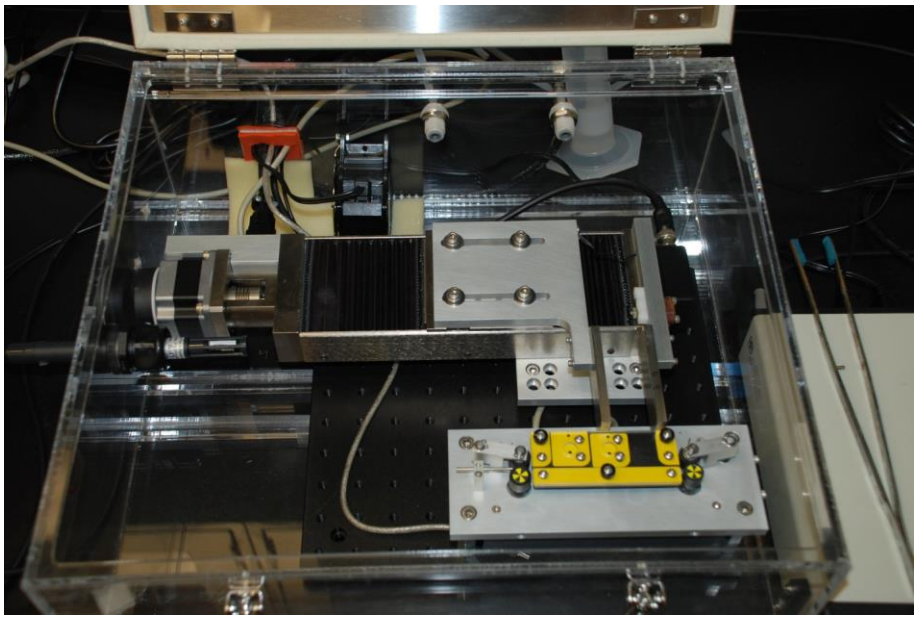

Figure 2-15. An image of the two point bend test setup used to evaluate strength at different loading rates and in different humidity environments.

In the first set of experiments, baseline strengths of the Nufern fiber were measured. This was done by conditioning a large length of fiber in the test enclosure under dry conditions (~0%RH) for a week. This was done to try and extract any moisture that might be trapped inside the polymer coating. Testing for the fiber was then completed at three different stressing rates, 5 MPa/s, 50 MPa/s, and 100 MPa/s, while keeping the conditions dry. Fifty strength tests at each loading rate were conducted. Figure 2-16 shows the strength distributions plotted using Weibull statistics.

The data clearly show that the strengths of the samples tested at the lower stressing rate are lower. It is postulated that despite our efforts to dry the polymer coating, some moisture remains in the structure. During slower rates of loading, migration of the polymer to the fiber surface, and a reaction with the surface to either grow the cracks or corrode the surface to form pit-like defects must be occurring to cause the lowered strength. The two higher loading rates lead to strength distributions that are nearly identical. Based on these results, the 50 MPa/s loading rate with one week of drying time at ~0%Rh was chosen as baseline, and results from fibers exposed to radiation were compared with this value. Another point to note from these data is the extremely high values of shape factors (~90-100) obtained for the fibers. This is indicative that defects that are intrinsic to structure of the glass are being sampled in these tests.

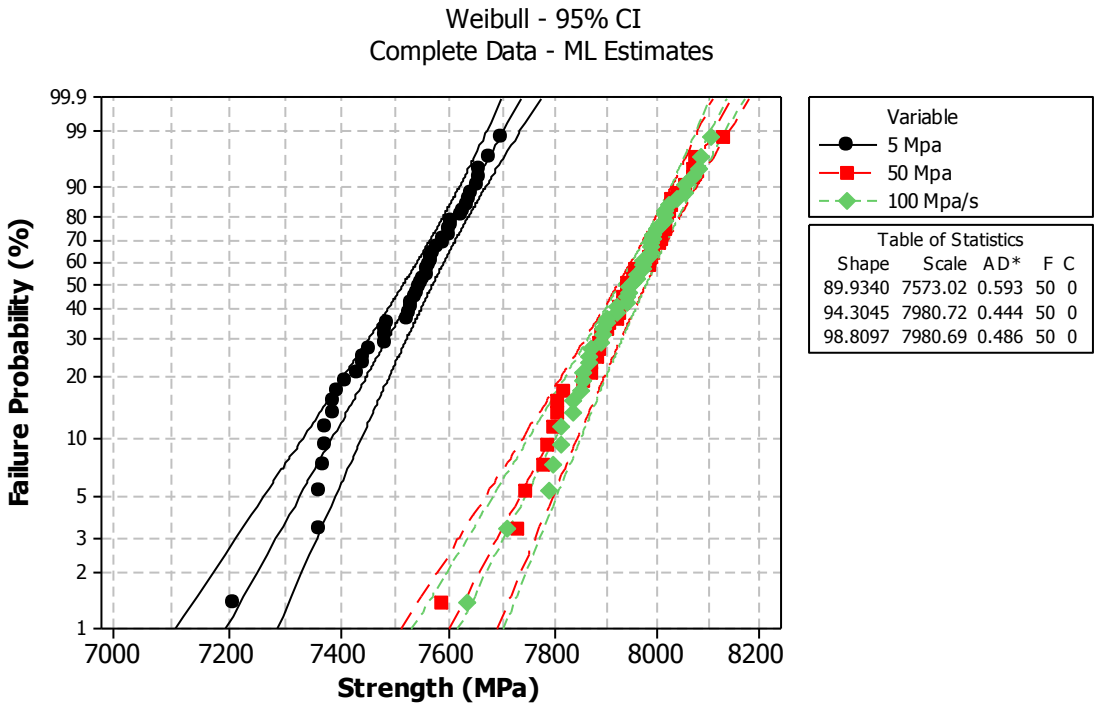

Figure 2-16. Strength distributions of fibers tested at different loading rates as fit to the Wiebull distribution.

The distribution parameters are included in the table of statistics.

2.2.2 Radiation Effects

Radiation effects on material properties are a very important implication for the use of the Fiber Optics in a particular space environment. There are several factors that need basic understanding for long term use in space; two of the most important are transmission "Insertion Loss" and strength reduction. First of all the insertion loss needs to fall inside a budget for transmission at end of life for the radiation environment expected. For a flexing device like the fiber optic, we would nominally design for use in a 100K Rad environment, essentially assuming the proper shielding to obtain this level of exposure. Secondly, the strength of the fiber will also be evaluated from the same samples. To fully bracket potential use of the fiber in space, radiation testing will be for transmission and strength across the range of environments from Table 1-1a.

An initial test for radiation effects took advantage of the strength test methods used for testing the fibers. Six spools of Nufern Multi-Mode GR-100/140-24HTA fiber were wrapped on spools in preparation for radiation testing. These could be left on the spool for fiber transmission testing, radiation exposure, post radiation fiber transmission, and finally strength measurement. In the image below one can see the fiber wrapped around Flight Kapton tape on the outside of a 7.5" diameter cardboard tube.

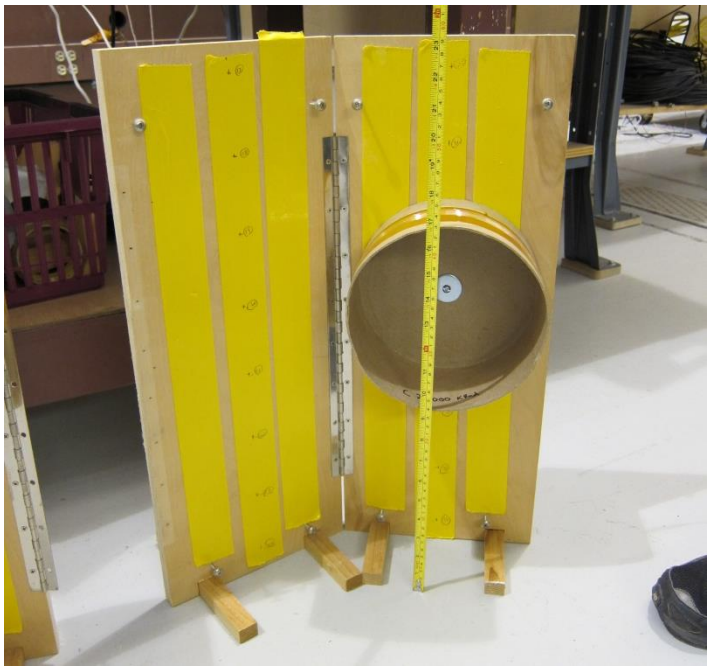

Figure 2-17. Radiation Support for GIF

The first two fiber samples were read with an Insertion Loss Meter (Laser 2000, OTDR OFM1020), in a random order to obtain repeatability on the transmission measurement and then retained as references without radiation exposure for a post radiation check. Results of that test shown in Figure 2-18 demonstrate that we get very repeatable results for the Insertion loss.

Measurement #	Cable	Insertion Loss (dB)	A	B
1	B	2.501	1.27	2.501
2	B	2.563	1.269	2.563
3	A	1.27	1.25	2.567
4	A	1.269	1.271	2.59
5	B	2.567	1.261	2.575
6	A	1.25	1.301	2.566
7	A	1.271	1.248	2.582
8	A	1.261	1.256	2.581
9	A	1.301	1.259	2.586
10	B	2.59	1.258	2.584
11	A	1.248		
12	B	2.575	Mean	Mean
13	B	2.566	1.26	2.57
14	A	1.256		
15	B	2.582		
16	B	2.581	Std Dev	Std Dev
17	B	2.586	0.0144	0.0244
18	A	1.259		
19	B	2.584		
20	A	1.258		

Figure 2-18. Radiation Reference Test

The next part of the test involved maintaining a control spool and three other spools of fiber for test. Each spool contained about 20 meters of fiber, which amount to about 4 strength samples of about 100 data points each. After consulting with the SNL GIF facility three exposures were set up to match our environmental requirements, one at 100 krad, a 5Mrad and a 24M Rad dose.

The following image shows the fibers set for the 24Mrad test dry cell radius of 70 cm, with the Cesium Gamma source deep in the pool during dry cell set up. The bluish color of the source is visible in the lower right corner of the image about 25 feet down in the pool of water. Once the fiber is placed at the test position, the dry cell is cleared and verified as closed; the Cesium source is raised out of the pool and lifted to the same level as the part under test to start the exposure. The personnel at the GIF know the exact configuration and rates and have arranged the sources to obtain our dose levels.

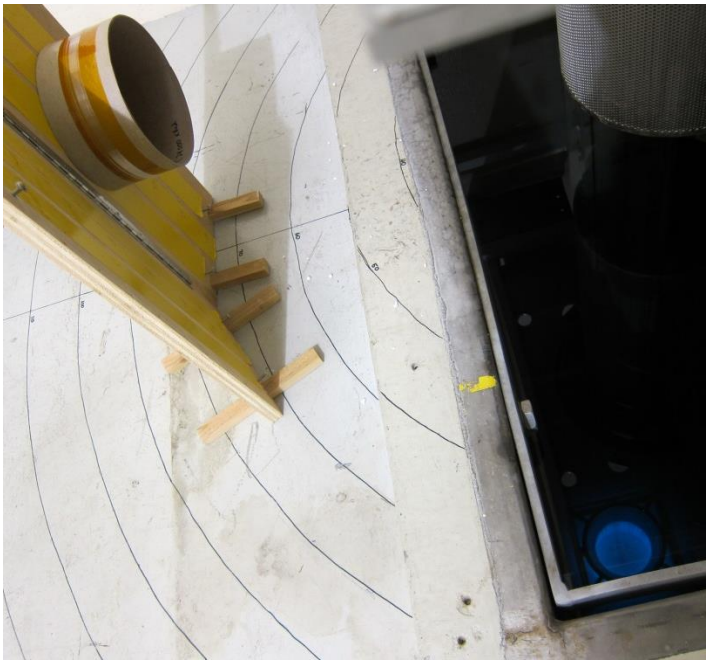

Figure 2-19. GIF 24Mrad Dry Cell Setup

Results of the exposure test for transmission are listed below and show very little degradation for a potential 1meter device. As you can see the 100 krad exposure had only about 0.36 dB/meter loss.

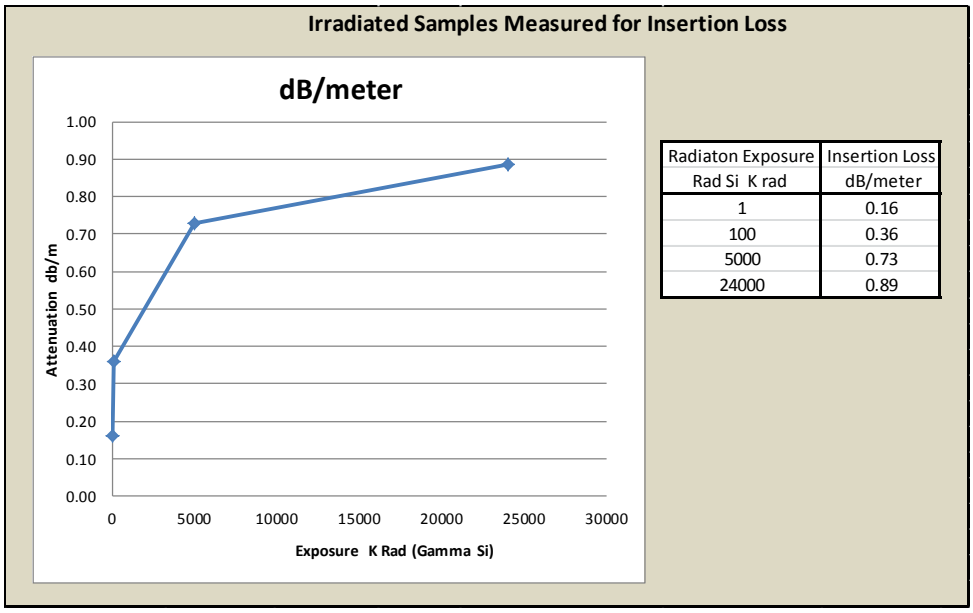

Radiaton Exposure Rad Si K rad	Insertion Loss dB/meter
1	0.16
100	0.36
5000	0.73
24000	0.89

Figure 2-20. Insertion Loss Radiation Exposure Results

Comparison to a budget for insertion loss of 0.36 dB from Figure 2-20 above is well below the budgeted amount of 5 dB. Clearly we meet the design needs with the 100krad shielding.

The other consideration for the radiation exposure is the strength of the fiber. After the transmission and radiation testing the fiber's strength was measured. As one can see in Figure 2-21, there was a drop in strength for the irradiated fibers, as compared to an optimum reference soaked in 0% RH for a week. The Black, "50MPa/sec after 1 week at 0%RH" is our reference. Sensitivity to moisture creeps into all of the results shown and great attention to the exact time %Rh needs to be considered.

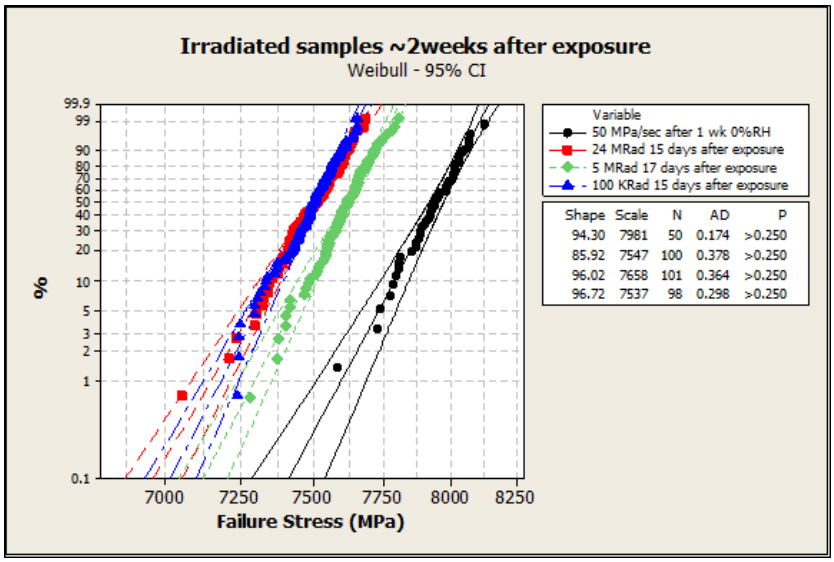

Figure 2-21. Irradiated Fiber Strength

Further review of the data allowed us to look at the strength over time. There was concern that there might be further degradation over time after the radiation exposure. Figure 2-22 shows results of testing of the same fiber at the same stress rate to failure at different intervals after testing.

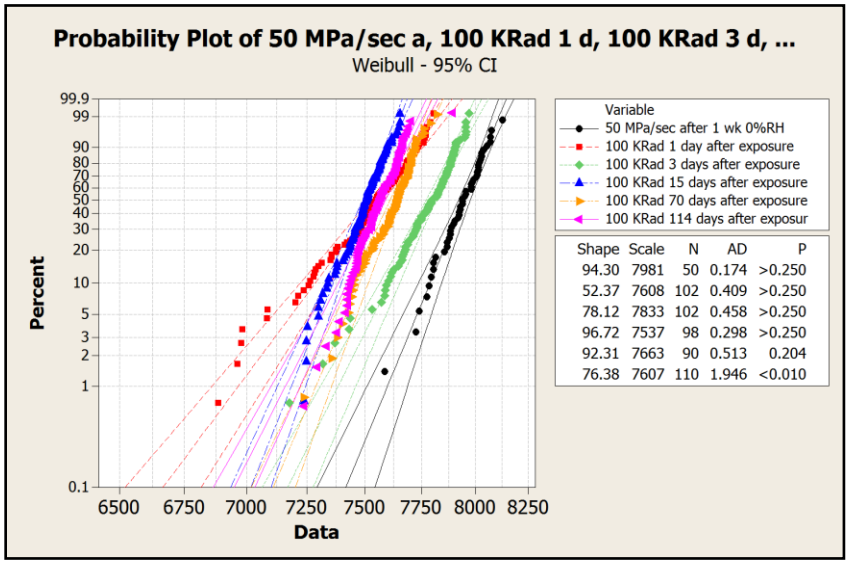

Figure 2-22. Irradiated Strength over Time

Clearly there is some variability in the strength, but no correlation to the time after test pattern. There was some thought that there might be a "healing" with time after exposure as seen in other materials. The 114 day test in magenta seems to contradict that for both the 70 and the 3-day test.

2.2.3 Stress Rate

Stress rate during testing will also have an effect on the measured strength of the fiber. Strength as measured on the two point bend strength tester were made with 50 data points at three different rates, see Figure 2-23. Slower rates do indicate a 5% lower strength. Review with the testing organization viewed the 50 MPa/sec after 1 week at 0% RH to be the baseline that we would compare against, our baseline.

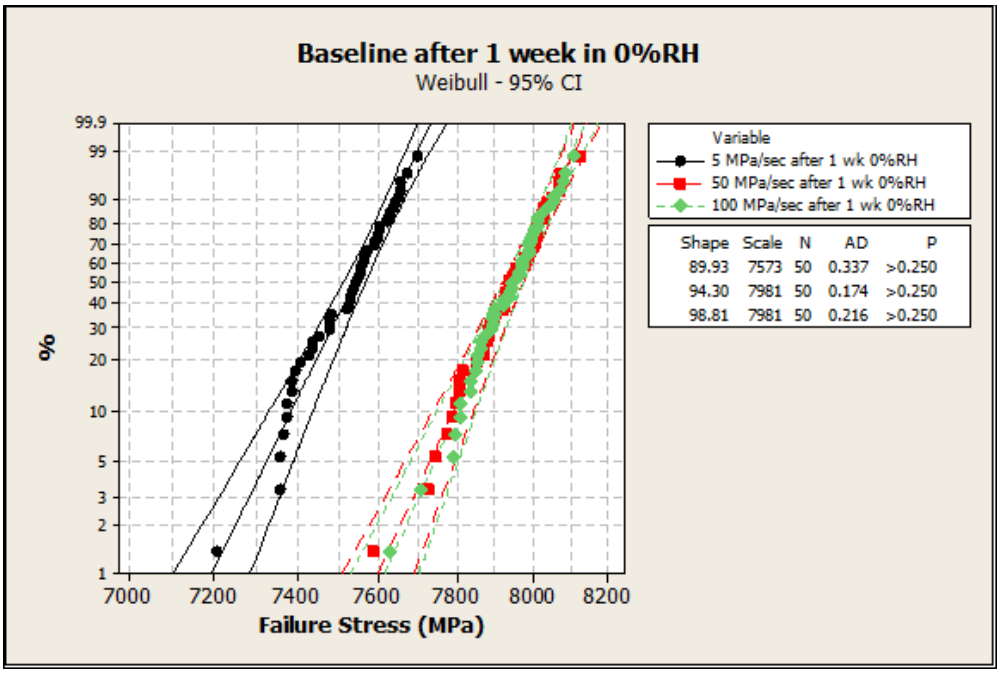

Figure 2-23. Baseline Testing at Different Stress Rates

2.2.4 Stiffness from Hardness

It is known that for optical fibers the core and cladding material differ in chemical composition. Fig. 2.1 shows the structure of the glass fiber, clearly showing the core and clad region. The clad region has a lower refractive index than the core, allowing for total internal reflection of the light, thereby allowing light to travel long distance in the pure core with minimal attenuation. For the fiber of interest here, the core is germanium-doped silica, and the clad is pure silica. The elastic modulus of the fiber is needed to calculate the stress at fracture from an applied bending strain in the two-point bend test described in Section 2.2.1. For measuring the elastic stiffness properties of small volumes, the nano-indentation technique can be utilized. A MTS XP nano-indenter (MTS Testing Systems, Eden Prairie, MN) has been used for our measurements. A schematic of the nano-indenter is shown in Figure 2-24.

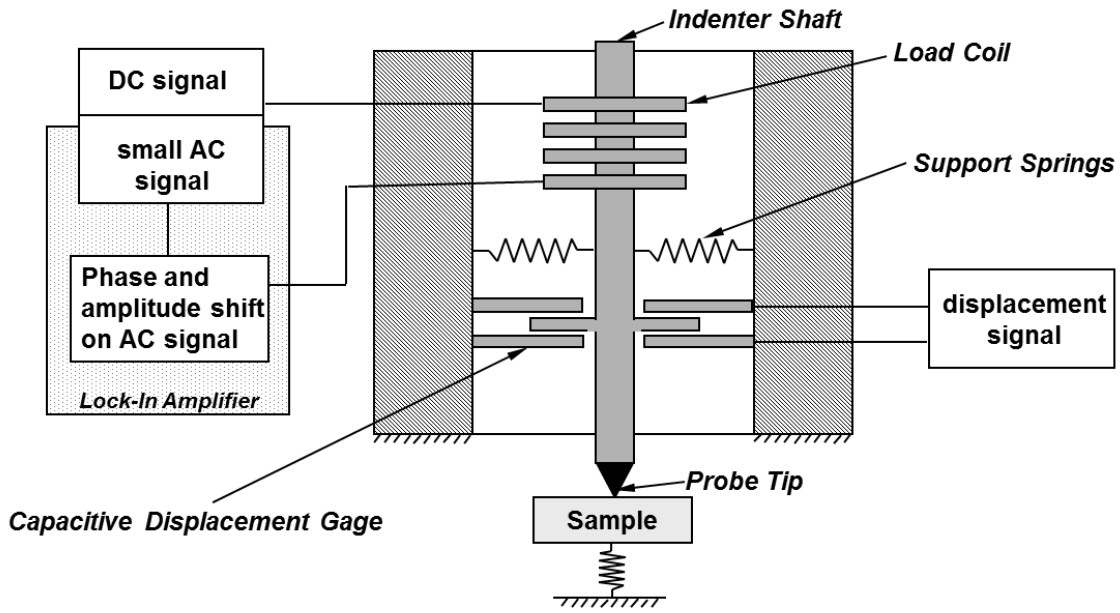

Figure 2-24. A schematic of the nano-indenter set up.

The sample is usually loaded with a three-sided diamond (Berkovich) tip, and the load and the displacement into the sample is continually monitored. The loading response in an indentation experiment is the result of combined elastic and plastic deformation of the material underneath the tip, while during unloading the elastic relaxation of the material as the tip disengages is measured. The unloading curve obtained from the experiment is fit to a polynomial in h (displacement). This fit is then differentiated by the displacement to obtain the unloading stiffness (S). The elastic modulus (E) of the material can then be calculated by:

$$E = \frac{\sqrt{\pi}}{2\beta}\frac{S}{\sqrt{A_c}}\frac{1}{\left(1-\nu^2\right)}$$

Equation 2-2-1

Where A_c is the contact area, β is a geometry ratio (~1), and ν is the Poisson's ratio of the material. The formulation also yields the contact depth, h, and the contact area needed for the calculation of E, as well as for the hardness. Further details of the formulation can be found in Oliver-Pharr, 1992.[10]

For our experiments, fibers were stripped from the polymer coating, mounted in hard epoxy and polished. The load resolution on our machine is ~1 μN, and the displacement resolution is 1-5 nm. Indentations were conducted to a depth of 250 nm using a Berkovich tip. Indents are spaced ~5um apart sampling the entire cross-section of the fiber. An image of one tested fiber is

[10]W.C. Oliver and G.M. Pharr (1992). An improved technique for determining hardness and elastic modulus using load and displacement sensing indentation experiments. Journal of Materials Research, 7, pp 1564-1583. doi:10.1557/JMR.1992.1564.

shown in Figure 2-25, where two rows of indentation placed on the fiber are visible. The indentations are placed such that both the core and cladding regions of the fiber are sampled.

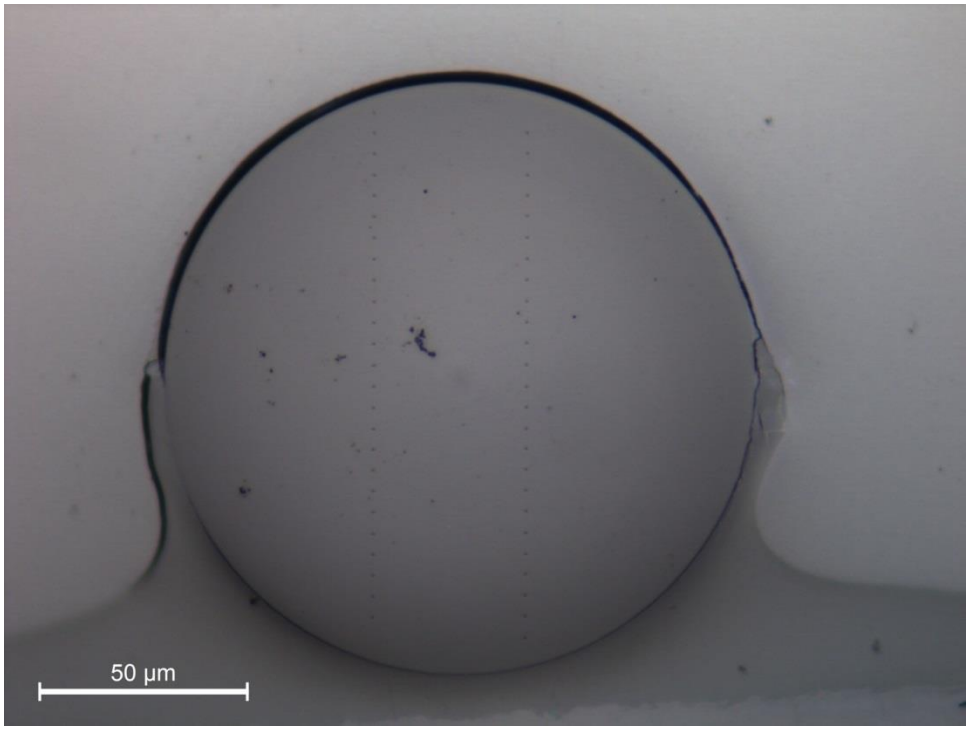

Figure 2-25. Image of a mounted section of fiber showing two rows of indentations for elastic modulus and hardness measurements.

The data as a function of location along the fiber cross-section were analyzed, and the results for elastic modulus and hardness are shown in Figure 2-26.

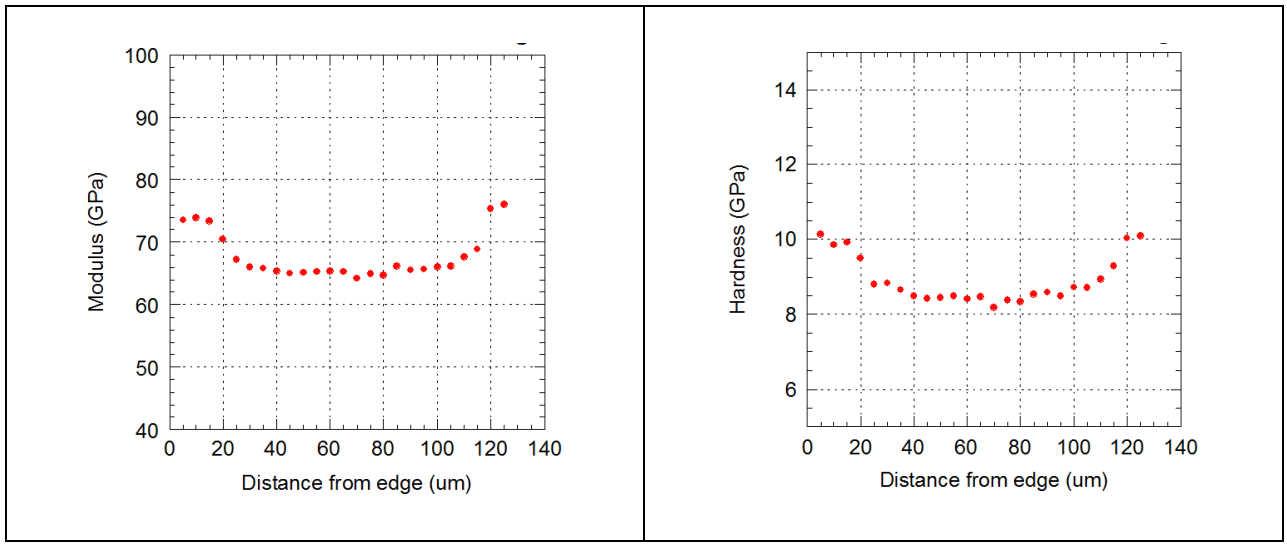

Figure 2-26. Elastic modulus and hardness as a function of location on fiber cross-section.

Note that 0 and 130 micron are the two ends of the clad region.

It can be observed that the elastic modulus of the silica clad is ~73 GPa, and nearly constant in the clad region. The modulus value dips down to ~66 GPa in the core, and then rises again as the indentation location traverses through the core to the clad region on the other side. A similar trend in hardness, with a value of ~10 GPa in the clad dropping down to ~8.5 GPa in the core is observed. This indicates that the germanium doped material exhibits slightly lower mechanical properties than the pure silica. The value of E obtained for silica can now be used in calculations to be described in Section 3.

2.3 Cyclic Testing

Cyclic testing was limited as funding for the effort was cut the second year of the LDRD. Testing took on the intent of using devices that would allow the two point tester to test the strength after cycling. We had three options and exercised them all. First was direct cycling in the two point tester, with a change of software from cycling to measuring the breaks/strength. The second was to use the MTS with the test jaws made for the bend force measurement. The third was a new design of a cylindrical tester that would expand a 6" diameter to 6.032 to give stress in the range of flight design levels.

Stress levels for the fiber in a flight environment would be limited to a minimum bend radius of 0.5 in (12.7mm) which results in 410 MPa stress based on 75 GPa Modulus from the outer glass fiber. A more nominal design bend radius of 1.0" (25.4mm) results in stress levels of 103 MPa.

2.3.1 Two Point Tester

The first method of test was simply to use 10 fibers on the two point tester. (See Figure 2-14 and Figure 2-15). Cyclic data would be limited in range but potentially useful since the two point tester has a very limited travel speed. 10 fibers could be cycled from 4.5 mm to 5.5 mm for a stress range of 0.9 to 1.1 Gpa for a stress ratio of 0.8 for about 20k cycles. Results are presented below in Figure 2-27 for dry and humid testing. In general we saw no degradation of strength with 20k cycles at 0% RH. The 22% RH showed a 20% decrease in strength from 7500 to 6000 MPa, at this test level. A repeat of this test near the design stress level would be prudent.

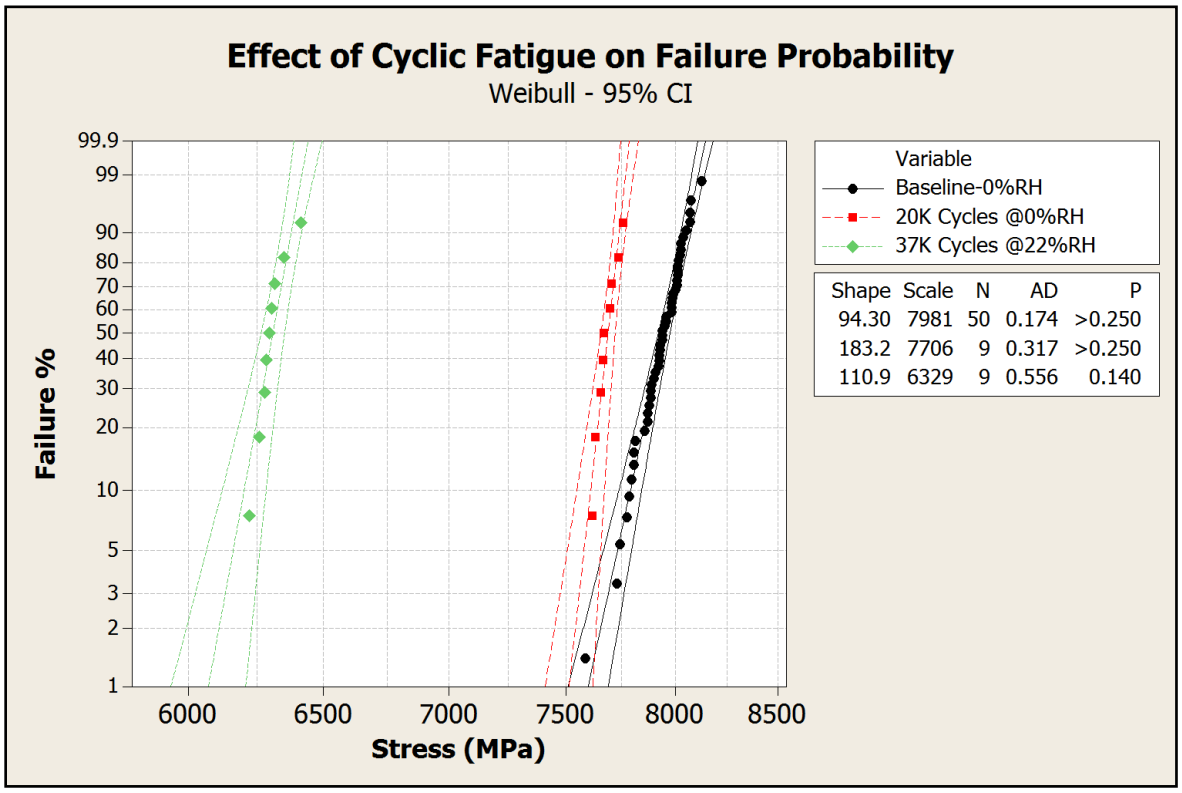

Figure 2-27. Cyclic Testing with a stress ratio of 0.8

2.3.2 MTS Tester

The MTS tester was also used as seen in Figure 3-10. The force gage was set up with 10 fibers that ran 20k cycles from 4.5mm to 7.5mm. An environmental box was set up and the fibers were dried to < 0.5 %RH. After 20k cycles the MTS was set up to slowly close until all the fibers broke, occurring at about 0.9 mm. This corresponds to a stress level of 5236 MPa at failure. Since all 10 break about the same time the Failure Probability cannot be calculated.

2.3.3 Cylindrical Test Fixture

The cylindrical tester required much more development. The concept would allow testing of a 10 meter sample, and was selected from several options as the tested fiber could easily be transferred to testing on the two point tester. An image of the device is shown in Figure 2-28.

Its intent was to do a quasi-tensile test with the 6” diameter as the bending stress at this diameter was very low at about 70 MPa, then be pumped up with about 3psi to get a stress level equivalent to a flight stress at about 500 MPa or a 0.35” bend radius.

In the upper-left corner of the image is the concept where a bladder is installed inside a cylinder with many slots to allow the center of the cylinder to expand with internal pressure. This fixture uses water as a hydraulic medium and an external piston to create a displacer. Going clockwise around the images is the cylinder with strain gages installed to measure the strain as the tester runs. In the lower right is a photo of the general setup and finally the lower left shows the complete mechanism, where an eccentric motorized disk drives an arm that in turn displaces the piston to give the proper amount of fluid volume to the cylinder.

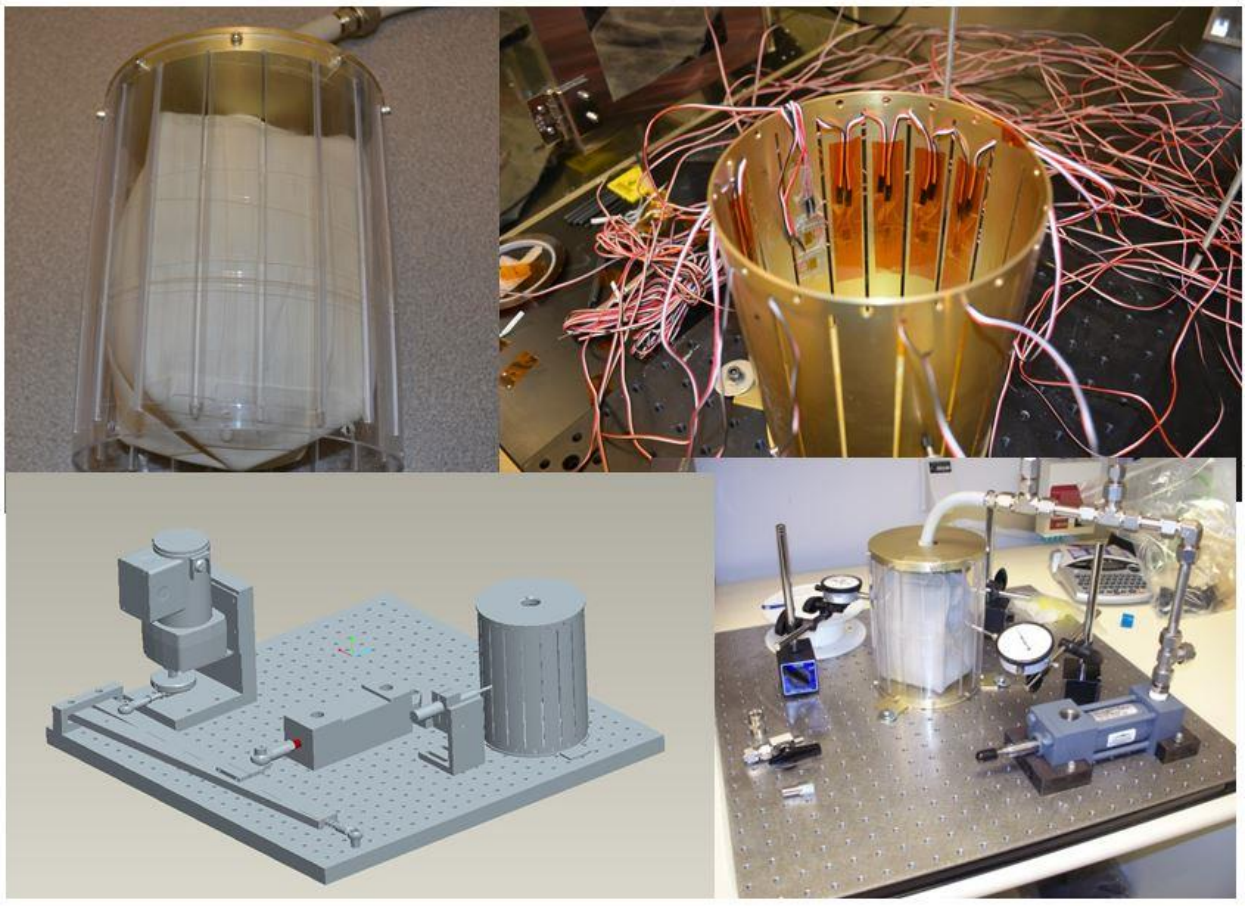

Figure 2-28. Cylindrical Tester

Included in the design was an analysis of the stresses in the cylinder since it had to go for millions of cycles. A design distortion of 0.015" radial growth in the cylinder was used as this got us to a 500 MPa stress level in the fiber

Below are the results for the fatigue test fixture with a 0.125" thick slotted AL6061 cylinder with #6-32 screws at top and bottom of every slat. An internal pressure of 3.125 psi was applied to the inner cylinder walls, and internal walls of the top and bottom plates. The bottom plate is fixed at the tabs. Because of symmetry, only half of the assembly was modeled and constrained so the model so it can't move out of plane of symmetry. The cylinder is attached to the top and bottom plates with rigid elements and stiff springs to calculate screw forces. The maximum radial displacement is 0.0151", compared to the desired 0.0165". The expected operating pressure will be somewhere between 3.0 and 3.25 psi and will have to be determined at the time of the test. Maximum stress is 11536 psi which is well below the 24,000 psi endurance limit of AL6061-T6. This stress is near a screw connection and is therefore probably not accurate. The maximum stress near the slots is 9847 psi; again well below the endurance limit so we should be able to run the fixture for many million cycles.

Add a section that shows the design margin/ fatigue estimate

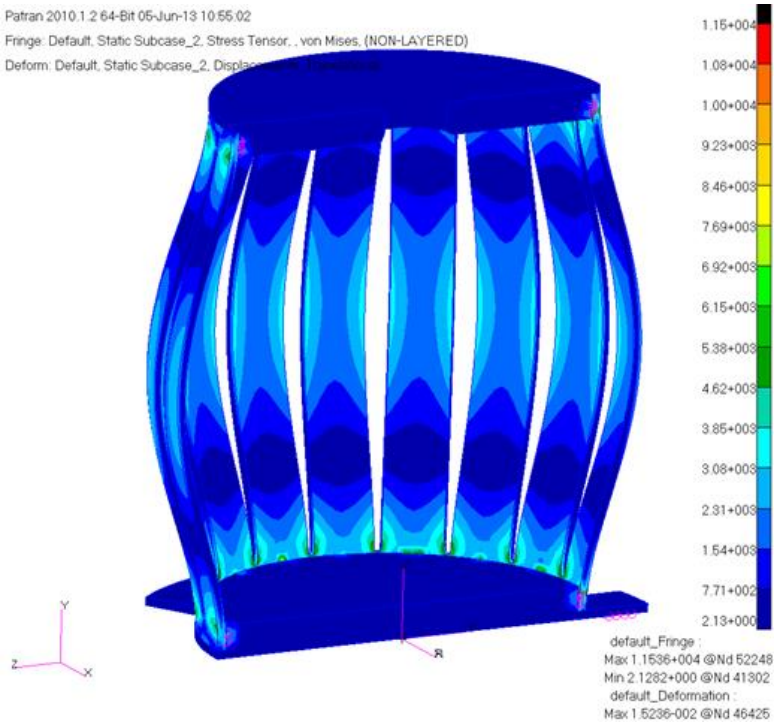

Figure 2-29. Von Mises Stress (PSI), Cylindrical Tester

A first run on the cylindrical tester had several outliers in the results as shown in Figure 2-30. We have seen these before and they were eliminated with alignment of the pinch points to be in the same plane. The technician feels these were from misalignment but unless he saw them occur it is hard to prove it was misaligned. Future runs will ensure alignment to secure consistent data.

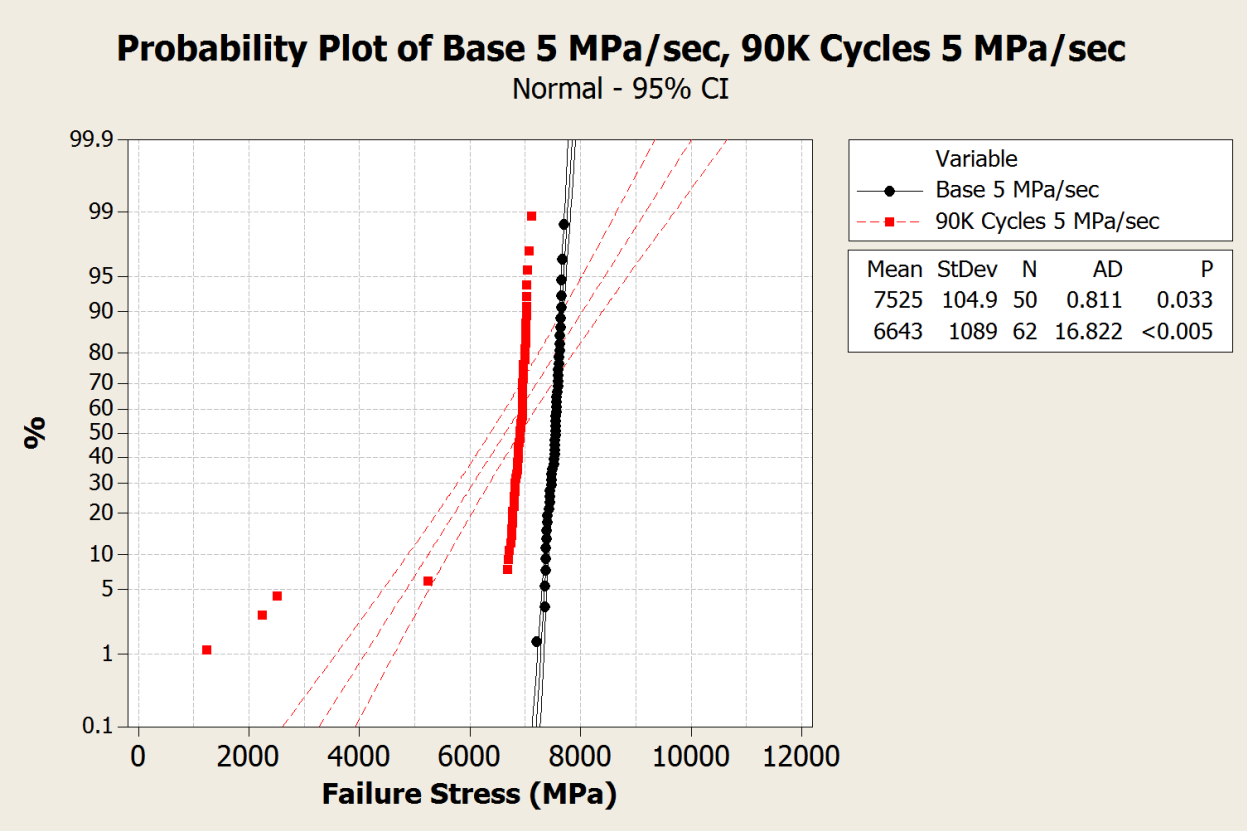

Figure 2-30. Cyclic Testing, Cylindrical Tester 0% RH

3 FIBER STRESS MODELING

3.1 Model Development

As discussed in Section 2.2.1 Strength Quantification, the optical fiber strength distribution was measured using the two-point bend tester designed by Matthewson, et. al. (1986)[11]. Measuring strength using two-point bending instead of uniaxial tension has the advantage that the fiber invariably breaks in the gage section, far away from the "grips". Uniaxial tension, on the other hand, measures the engineering strength directly, while two-point bending requires a model to interpret the results. Here we built a simplified model of the two-point bend test to connect the maximum stress in the fiber to the measured faceplate separation.

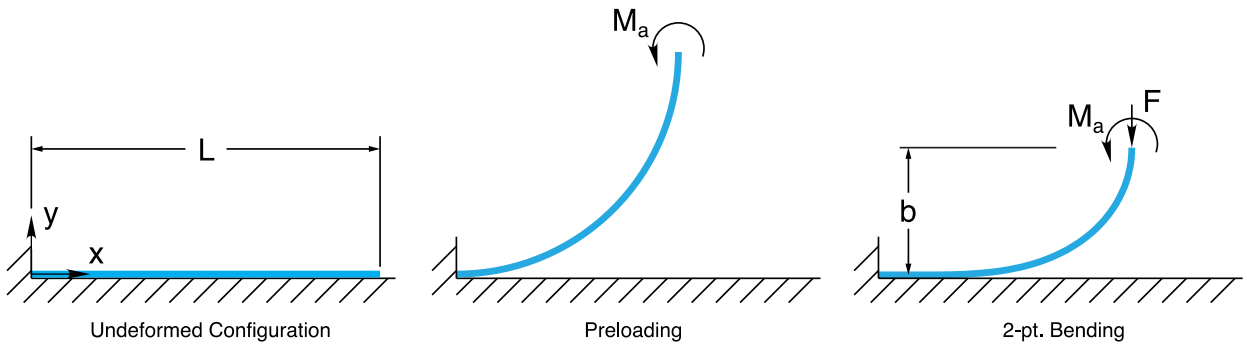

Figure 3-1. Two-Point Bending Simulation Procedure

The general sequence of a two-point bending simulation can be seen in Figure 3-1. In the undeformed configuration, the fiber is straight, has the length L = 23.56 mm, and lies on top of the rigid faceplate. The left end of the fiber is rigidly fixed to the left wall. During preloading, the fiber is bent into a 90-degree circular arc by the moment M_a at the apex of the fiber. After preloading, it should be clear that we are modeling only half the fiber arc, i.e. the fiber shape is assumed to be symmetric about the apex. During two-point bending, the moment M_a is adjusted to hold the apex rotation fixed and a small force F pushes the apex downward. This force causes a portion of the fiber to come into contact with the bottom faceplate as the distance b decreases. (The faceplate separation is $2b$ plus the outer diameter of the secondary coating d.)

[11] "Strength Measurements of Optical Fibers by Bending", M.J. Matthewson and Charles R Kurkjian, J. Am. Ceram. Soc., 69 [11] 815-21 (1986)

Gulati (1981)[12] modeled the two-point bending process in Figure 3-1 using Elastica theory. (See Matthewson et. al. (1986) for a summary of Gulati's model, and see Levien (2008)[13] for a review of Elastica theory.) By treating the fiber as a homogeneous, linear elastic, material, Gulati found an analytical solution for the maximum strain at the apex of the fiber ε_a, as a function of the distance *b*,

$$\varepsilon_a(b) = \sqrt{\frac{2}{\pi}}\,\Gamma\left(\frac{3}{4}\right)^2 \frac{r}{b}$$

Equation 3-1

where $\Gamma(x)$ is the Euler gamma function and *r* is the undeformed radius of the glass fiber cross-section. The Euler gamma function is defined as

$$\Gamma(x) = \int_0^\infty t^{x-1} e^{-t}\, dt,$$

so Equation 3-1evaluates to

$$\varepsilon_a(b) = 1.19814\,\frac{r}{b}.$$

Equation 3-2

Defining *E* as the modulus of the fiber, the maximum stress at the fiber apex σ_a is

$$\sigma_a = E\,\varepsilon_a = 1.19814\,E\,\frac{r}{b}$$

Equation 3-3

Gulati's analysis also affords an expression for the contact force F as a function of *b*,

$$F(b) = \frac{1}{\pi}\,\Gamma\left(\frac{3}{4}\right)^4 \frac{E\,I}{b^2} = 0.71777\,\frac{E\,I}{b^2}$$

Equation 3-4

where *I* is the area moment of inertia of the fiber cross section.

We elected to create a finite element (FE) model of the two-point bending test rather than rely on Gulati's model for several reasons. First, Gulati modeled the contact force between the fiber and

[12] "Nonlinear Bending of Strong Glass Fibers", S.T. Gulati, for abstract see Am. Ceram. Soc. Bull., 60 [8] 862 (1981)
[13] "The elastica: a mathematical history", R. Levien, UCB/EECS-2008-103, Aug. 2008

the bottom faceplate as a single point load instead of a distributed load and assumed the moment was zero at the point of contact. Consider a cantilever beam of length *L*, where one end is built into a wall and the other end has a transverse point load *F*. At the wall, the moment is *F L* and the curvature is nonzero. At the other end, the moment and curvature are zero. In our case, we were not certain which boundary condition prevailed at the point of contact between the fiber and the faceplate. Second, the assumption of linear elastic material behavior is crucial to obtain Gulati's analytical solution. We did not want to be constrained to linear elastic material models for the glass fiber or the polymer coatings. Third, the boundary conditions that cause the fiber to deform into a "U" – shape in the model may not be an accurate representation of the conditions produced by the two-point bend tester auto-loader. An auto-loaded fiber usually looks more like an "Ω" - shape (see Figure 3-2) rather than a "U" – shape. Perhaps the Elastica theory could represent the "Ω" - shape, but a FE model is more likely to have the necessary capability. Due to funding reductions, we did not exercise the extra flexibility of the FE model to investigate the impact of a non-linear material model or the "Ω"- shape, but the capability may be useful in future studies.

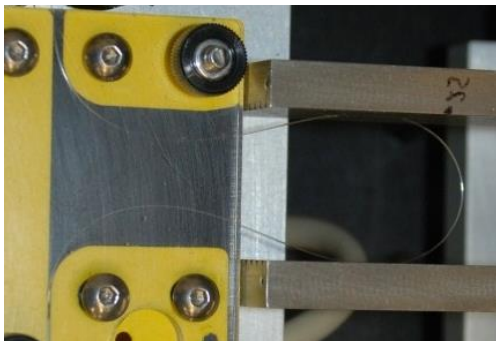

Figure 3-2. Fiber auto-loaded into the two point bend tester.

The fiber was modeled using a series of two-node, Timoshenko type, beam elements in Sandia's finite element code, Sierra/SM quasi-statics (Sierra/SM Team, 2013). Beam elements are computationally efficient for slender geometries such as the optical fiber and they allow the analyst to easily prescribe moment/rotation boundary conditions. The number of beam elements was chosen from the mesh convergence study detailed below. The faceplate was modeled using rigid 8-node hexahedral brick elements. Contact between the fiber and faceplate was handled using the Sierra/SM's DASH search algorithm and the Augmented Lagrange method for contact enforcement. The contact interface was treated as frictionless for simplicity, but the amount of sliding was negligible due to the nature of the boundary value problem.

The stress vs. strain response differs between the core, cladding, and polymer coatings, so three different models of increasing complexity were pursued. In model A, the core and cladding were treated as one homogeneous material and the polymer coatings were ignored. The elastic modulus of 72.0 GPa in Table 3-1 is the commonly accepted value for silica in the published literature. In model B, the core and the cladding were modeled individually, each with their own elastic modulus. The modulus of 65.6 GPa for the core is the average of the central 20 to 115 mm region in the left plot of Figure 2-26 and the 17 to 112 mm region in the right plot of Figure 2-26. The value of 74.4 GPa for the cladding is the average of the remaining data points in Figure 2-26. In model C, the secondary polymer coating was added to the model without the

primary coating. The composite 0.410 GPa modulus in Figure 2-3 was treated as the modulus of the secondary coating in isolation, because the primary coating is rubbery at room temperature, while the secondary coating is glassy at room temperature.

The materials in all three models were assumed to be linear elastic for simplicity. Although silica is known to have a slightly non-linear elastic stress vs. strain behavior (Krause, 1979)[14], it is frequently ignored as a first order approximation. Future investigators may wish to examine the impact of silica's non-linear behavior. The polymer coatings also exhibit non-linear (viscoelastic) behavior, but we expect the coating stiffness to be insignificant compared to the glass. To test this expectation, we purposely overestimated the secondary coating stiffness by treating it as a linear-elastic material. If the contribution of a linear-elastic secondary coating is small, then the contribution of a non-linear viscoelastic secondary coating will be negligible.

	Core (GPa)	Cladding (GPa)	Primary Coating (GPa)	Secondary Coating (GPa)
Model A	72.0	72.0	0	0
Model B	65.6	74.4	0	0
Model C	65.6	74.4	0	0.410

Table 3-1. Linear elastic moduli for various materials and models

The three models all used the manufacturer's nominal values for the core, cladding, and secondary polymer coating outer diameter. The manufacturer did not provide an outer diameter for the primary coating (or an inner diameter for the secondary coating) so a value of 195μm was estimated from Figure 2-1. The outer diameter of the secondary coating is d = 245 μm. See Table 3-2 for an explicit list of cross section dimensions.

	Core	Cladding	Primary Coating	Secondary Coating
Inner Diameter (μm)	N/A	100	140	195
Outer Diameter (μm)	100	140	195	245

Table 3-2. Cross-section dimensions used in the simulations

3.2 Model Validation

3.2.1 Initial Assessment

Figure 3-3 and Figure 3-4 provide a broad view of a two-point bending simulation using Model A. This simulation used a uniform mesh with an element length of $h = L/240$. In the early experimental work of Section 2.2.1 Strength Quantification, fibers broke at a centerline-to-centerline distance of approximately $2b$ = 1.8 mm, so the simulation was halted at this value.

[14] "Deviations from linearity in the dependence of elongation upon force for fibers of simple glass formers and of glass optical lightguides", J. T. Krause, L. R. Testardi, and R. N. Thurston, Physics and Chemistry of Glasses, Vol. 20, No. 6 (1979), pp. 135-139

The curves labeled with circled numbers in Figure 3-4a, b, and c correspond to the circled number instances in Figure 3-3 and Figure 3-5.

Figure 3-3 shows that once 2*b* reaches approximately 6 mm the total contact force on the faceplate *F* quickly increases to a final value of 1.2 N. This rapid ramp in force is consistent with the fiber shapes plotted in Figure 3-4a. At instance ①, the fiber experiences a mild bend and the contact force is small, but the bend and the contact force become much more severe by ⑦. Figure 3-4b plots the maximum bending stress σ against the undeformed position along the fiber *S*. As expected, σ is greatest at the fiber apex, where $\sigma = \sigma_a$. Note that the final bending stress of 6.71 GPa makes the final axial stress of 0.06 GPa due to the contact force *F* insignificant.

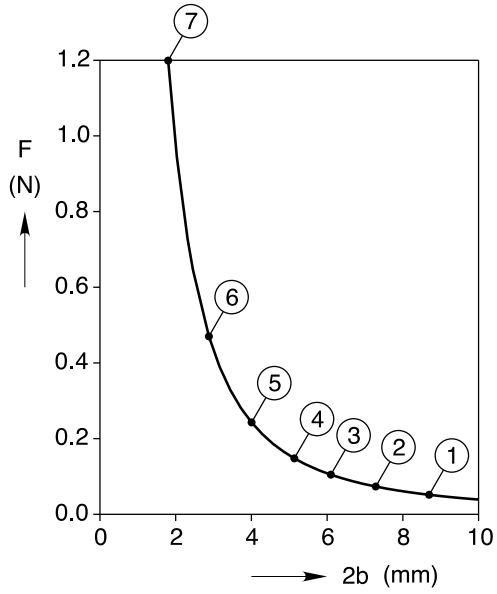

Figure 3-3. Total contact force *F* versus fiber centerline-to-centerline separation.

Circled number instances correspond to the curves in Figure 3-4 and the instances in Figure 3-5.

In all instances, the contact force distribution *P* is very sharp in Figure 3-4c, which validates Gulati's assumption that the contact forces can be modeled as a point load. The contact force distribution *P* was calculated by dividing the contact force at each FE node by the element length *h*. (The total force *F* is simply an integration of *P* over the length of the faceplate.) A point load generates no moment about its point of application, so the sharp distributions in Figure 3-4c also explain why σ is zero at the point of contact in Figure 3-4b.

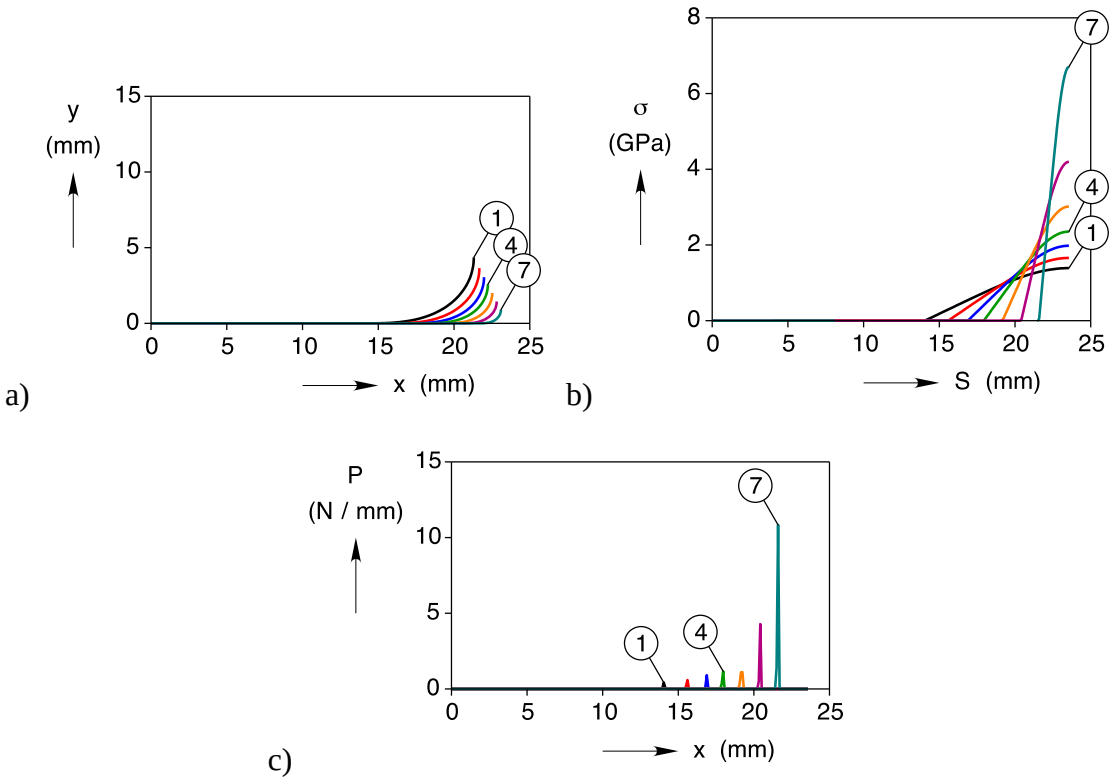

Figure 3-4. Field results. (a) Fiber shape, (b) bending stress distribution, (c) and contact force distribution at various times during the simulation.

Curves correspond to the circled number instances in Figure 3-3 and Figure 3-5.

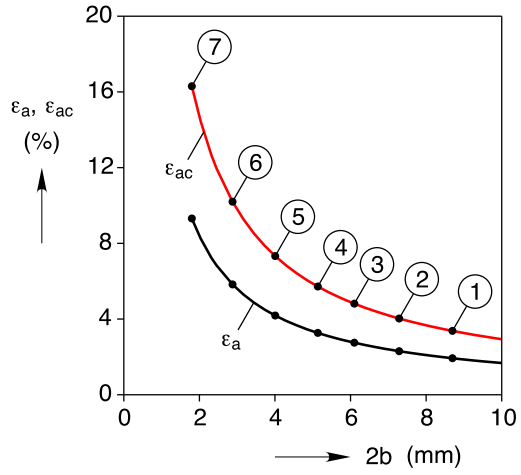

Figure 3-5. Maximum strain in the silica ε_a and maximum strain in the secondary polymer coating ε_{ac} versus the fiber centerline-to-centerline separation.

Circled number instances correspond to the curves in Figure 3-4 and the instances in Figure 3-3.

Figure 3-5 demonstrates that the maximum strain in the silica ε_a and the maximum strain in the secondary polymer coating ε_{ac} are quite large. Judging from the stiffening in the stress vs. strain curve in Krause (1979) and the magnitude of ε_a, non-linear material models for the silica may be worthwhile in future work. The large strains in the secondary polymer coating suggest it may experience permanent damage prior to total fiber failure in two-point bending. While important to keep in mind, damage to the polymer coating likely has a small impact on the silica stresses during two-point bending. Furthermore, the expected fiber service strains are several factors 10x (2b=50mm) less than those seen in two-point bending.

Figure 3-6 examines the behavior of Model A as the FE mesh is refined. Five simulations with five different element lengths $h = \{L/15,\ L/30,\ L/60,\ L/120,\ L/240\}$ are compared against the Gulati (1981) model. All simulations utilized uniform meshes. Figure 3-6a plots the maximum bending stress at the apex of the bent fiber σ_a against the fiber centerline-to-centerline distance$2b$. As might be expected from the b in the denominator of Equation 3-2, the bending stress σ_a quickly ramps up as $2b$ decreases. Finer mesh ($h = \{L/60,\ L/120,\ L/240\}$) results are virtually indistinguishable in Figure 3-6a and match up very well with the Gulati model. Figure 3-6b provides a closer view of the percent difference e between the FE simulations and the Gulati model at $2b$ = 1.8 mm. Element lengths of $h = \{L/60,\ L/120\}$ might be considered sufficiently converged for most practical situations. On the other hand, beam element simulations are not computationally intensive, so we elected to use an element length of $h = L/240$ for all further simulations.

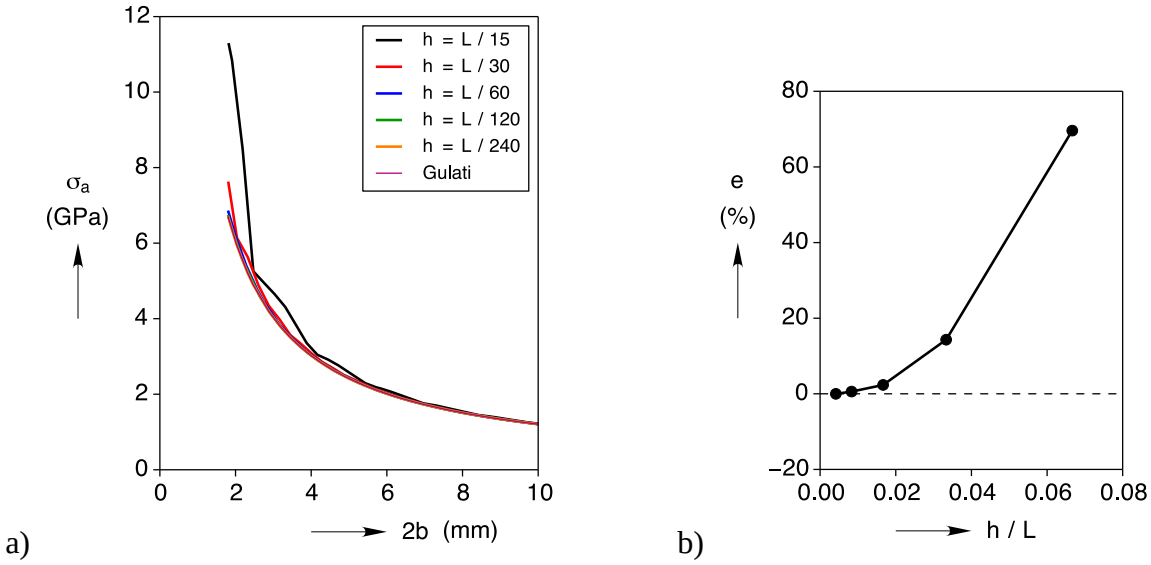

Figure 3-6. Mesh convergence of Model A to the Gulati (1981) model.

(a) Maximum bending stress as a function of fiber center-to-center distance.
(b) Percent difference between the FE solutions and the Gulati model for the maximum bending stress at $2b$ = 1.8 mm

The core, cladding, and secondary polymer coating are all modeled as linear elastic materials, so a relatively simply analysis can be used to calculate the response for Model B and Model C. Gulati found that the bent shape of the fiber, for a given value of *b*, is independent of the fiber bending stiffness $E\,I$ (see Eqn. (7) in Matthewson et. al. (1986)), where *E* is the modulus of the silica and *I* is the area moment of inertia. Gulati only considered a homogeneous cross-section fiber, but his analysis still applies to Model B and Model C, because the fiber still has a linear moment-curvature relationship. One can construct an effective bending stiffness $(E\,I)_{eff}$, such that the moment *M* is still linearly related to the curvature κ

$$M = \left(E_1 I_1 + E_2 I_2 + E_4 I_4\right)\kappa = \left(E\,I\right)_{eff}\,\kappa$$

Equation 3-5

where $E_1\,I_1$, $E_2\,I_2$, and $E_4\,I_4$, are the bending stiffnesses of the core, cladding, and secondary coating respectively. Because the bent shape of the fiber (Fig. 3b) is the same for all three models, the bending stress at the outer diameter of the cladding can be calculated as

$$\sigma_a = E_2\,\varepsilon_a = E_2 1.19814\,\frac{r}{b}$$

Equation 3-6

where E_2 is the modulus of the cladding. Similarly, the contact force *F* can be calculated by replacing $E\,I$ in Equation 3-4 with $(E\,I)_{eff}$,

$$F(b) = 0.71777\frac{\left(E\,I\right)_{eff}}{b^2}$$

Equation 3-7

The three models are compared in Figure 7. The differences between model A and model B are negligible, because the measured core and cladding moduli are not significantly different from the commonly accepted value of 72.0 GPa. The differences between model B and model C are also negligible. Despite the larger moment arm of the secondary coating, its stiffness is too small compared to the silica to make a significant impact. In view of these results, Model A will be utilized from here forward.

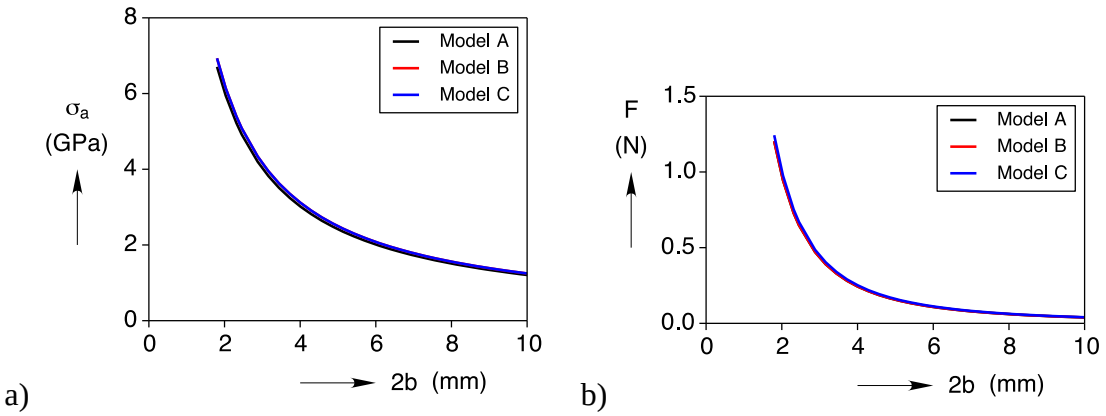

Figure 3-7. Comparison between Model A, B, and C.

(a) Maximum bending stress vs. fiber center-to-center distance.
(b) Contact force vs. fiber center-to-center distance.

3.2.2 Experimental Validation

Model A was validated against two experiments. First, the shape of the bent fiber was compared against photos taken of the specimen during two-point bending. Second, the predicted contact force F was compared to a load cell connected to the faceplate.

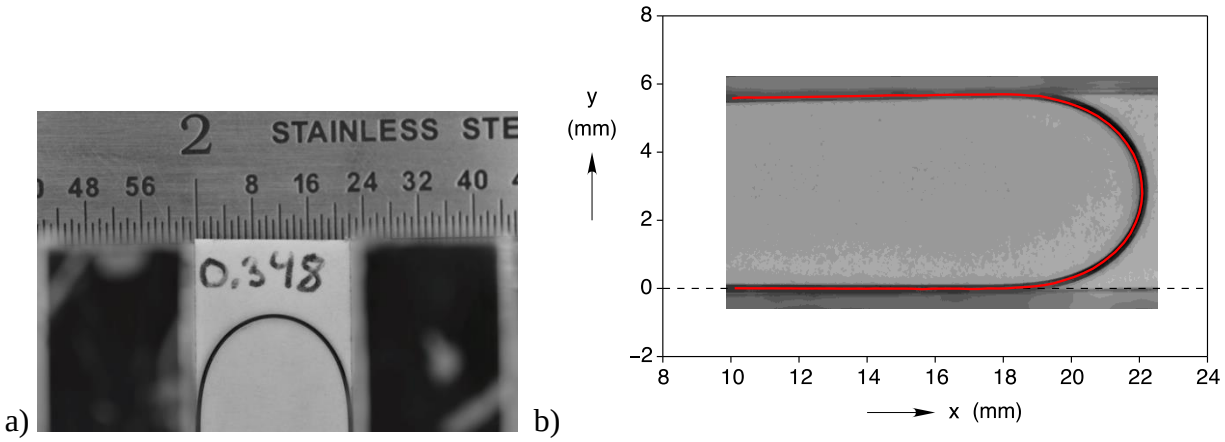

Figure 3-8. Fiber edge detection.

(a) An image of the fiber in-between jaws of a vice, with a ruler for scale.
(b) Edge detection results (red) overlaid on the image of the fiber (gray scale) for a fiber centerline-to-centerline distance of $2b$ = 5.70 mm.

The following procedure was used to capture photos of the fiber bent in a two-point bending configuration. The translucent fiber was first covered in black ink using a sharpie pen. It was then bent into a "U"-shape and placed on top of a white piece of cardboard between the smooth jaws of a drill press vice. The vice sat upon a table, and a camera stand was used to support a

Nikon D-5200 camera with a 4000 x 6000 pixel CCD sensor and a 60mm AF Micro Nikkorlens. The camera f-stop and exposure time were set to 4.8 and 13 seconds, respectively. Ambient lighting was sufficient to illuminate the specimen. Once the camera was focused on the fiber, the vice was moved downward. A stainless steel ruler with 1/64" increments was placed across the vice jaws, and the photo in Figure 3-8a was taken. (This photo was later measured to establish that 217.6 pixels were equivalent to 1 mm.) From this point forward, the position, the f-stop, and the exposure time of the camera were not altered until the after the experiment. Next, the vice was moved back up so that the fiber filled the field of view, and a photo was taken. The fiber was then removed from the vice without disturbing the white cardboard or the position of the vice, and another photo was taken. The vice jaws were adjusted to accommodate a new piece of cardboard with a different width, and another pair of photos with and without the bent fiber were taken. This process was repeated for a total of five different fiber centerline-to-centerline separations $2b = \{5.70\text{ mm}, 6.94\text{ mm}, 8.70\text{ mm}, 11.68\text{ mm}, 16.94\text{ mm}\}$.

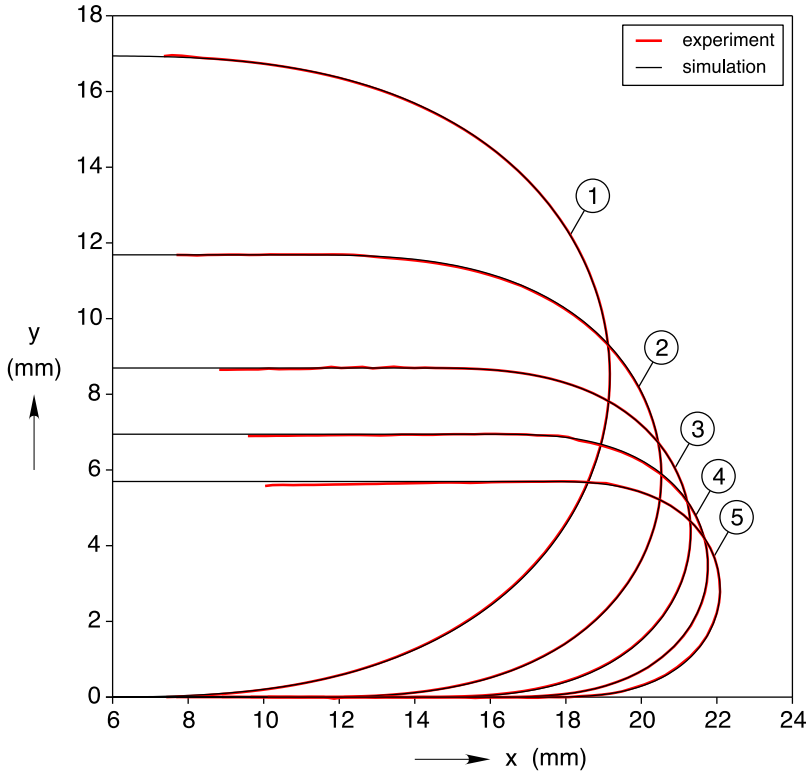

Figure 3-9. Comparison between the edge detected fiber centerline to the simulation predicted fiber centerline for five different fiber centerline-to-centerline separations.

The circled numbers for each pair of curves correspond to the circled number instances in Figure 3-11.

The ten photos were then loaded into Matlab (2013), where the following steps were taken to find the fiber centerlines.

1. The color photos were converted to 8-bit gray scale images.

2. The background image (without the fiber) was subtracted from the fiber image to remove spurious background noise that might get detected as edges.
3. A threshold was applied to the subtracted image, such that gray level values less than 70 were set to 0.
4. Edges (high contrast gradients) in the image were detected using the Canny method inside the Matlab function "edge()".
5. The edges corresponding to the inner curve of the fiber silhouette were identified.
6. The fiber centerline was found by offsetting the inner curve by half the undeformed fiber cross-section diameter d.

Originally, we attempted to find the fiber centerline by "radially" averaging the inner and outer edges of the fiber silhouette. This method worked well along the bent section of the fiber, but it performed poorly near the vice jaws where the outer edge of the fiber were difficult to detect. Instead, we elected to simply offset the inner edge by $d/2$ because the inner edge of the fiber remained detectable near the vice jaws.

An example typical of the results from this method are shown in red in Figure 3-8b for $2b$ = 5.70 mm.

The bent shapes of the fiber predicted by the simulations match up very well with the edge detection measurements, as shown in Figure 3-9. The favorable agreement demonstrates that Euler's Elastica theory is a good representation of the fiber bending behavior for the range of bent shapes compared.

Each of the simulation results is labeled with a circled number in Figure 3-9, which correlates the bent shapes with the contact force predictions in Figure 3-11. Strictly speaking, the two experiments cannot be directly correlated in the same manner because they were performed separately and on different specimens. On the other hand, there is no reason to expect the photos and load measurements would be significantly different if they were gathered during the same experiment. Specimen to specimen variability is minimal, and the fiber centerline-to-centerline separation serves as the link between the two sets of experimental data.

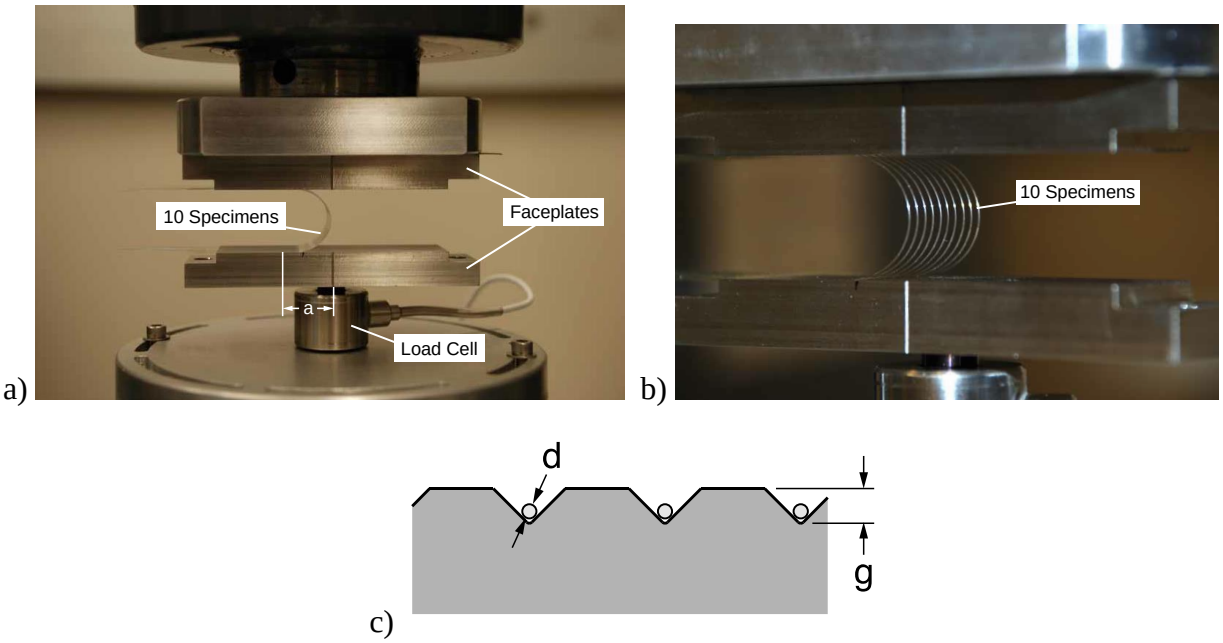

Figure 3-10. Setup for the contact force experiment. (a) A frontal view of the setup. (b) A closer, oblique, view of the fibers in the setup. (c) Fibers sitting in faceplate grooves.

The setup for the contact force experiment is displayed in Figure 3-10. Preliminary modeling results predicted that one fiber would break when the contact force F reached roughly 1.2 N (at 0% humidity). Instead of attempting to measure such a small force, a 5 Lb. capacity load cell (manufacturer Honeywell, model 31 (PN 060-1434-05)) measured the force Q due to bending 10 fibers at once. We then calculated the contact force as $F = Q/10$. Figure 3-10 shows the 10 fibers in-between two faceplates attached to a MTS servo-hydraulic load frame (system #507355)). The stainless steel faceplates were custom made to have the same "V"-shaped grooves as those in the two-point bend tester shown in Figure 3-2. The groove depth in Figure 3-10 was measured as g = 0.609 mm. The grooves helped align the fibers, so that each fiber's bending plane was parallel to the others. Special care was taken to slide each fiber along its respective grooves until all the fiber bend apexes aligned at the same x-location. A linear variable differential transformer (LVDT) measured the distance D between the top faceplate and the bottom stationary faceplate during the experiment. The fiber centerline-to-centerline distance $2b$ was calculated afterwards as

$$2b = D + 2g - \frac{d}{\cos\left(45^{\circ}\right)}$$

Equation 3-8

where $d/(2\ \cos(45^o))$ is the distance from the bottom of the groove to the fiber centerline.

The nature of the two-point bend test causes the contact point between the fiber and the faceplate to move. At the start of the test, the fibers contacted the faceplates at a distance of a = 17.5 mm from the load cell axis (see Figure 3-10a). During the test, the fiber-to-faceplate contact point

moved towards the load cell axis until the fibers broke, where the contact point was approximately above the load cell.

Off-axis loads generate moments that can alter load cell readings, but we found that our load cell was relatively insensitive to the off-axis loads in this experiment. A weight of 4.87 N was placed on top of the bottom faceplate at five different locations ranging from directly above the load cell to 38.5 mm away from the load cell axis. The percent difference between the weight and the load cell measurement was calculated at each location. The maximum percent difference was 0.4% for an applied moment of $(4.87\text{ N})(38.5\text{ mm}) = 187$ N-mm. We do not have exact measurements of the moment in the experiment, but we can take the maximum load of 6.43 N (when the fiber broke) and place it the contact point starting point (a = 17.5 mm). This very conservative worst case produces a moment of only 113 N-mm.

The measured contact force is plotted against the fiber centerline-to-centerline distance in Figure 3-11. The sharp drop in experimentally measured load at $2b$ = 2.30 mm and F = 0.631 N is due to the fibers breaking in the open air. Had we tested the fibers in a dry environment, the fibers would have broken closer to $2b$ = 1.8 mm. At the time of the test, the ten fibers broke from one side to the other in order, instead of randomly. This is likely the reason the load does not instantaneously drop to zero at $2b$ = 2.30 mm. One might suspect that the faceplates were slightly misaligned, but a measurement of the coplanarity of the two faces was made using feeler gages and it was on the order of 0.001".

The experimentally measured contact force is compared against the simulation prediction in Figure 3-11. The simulation and experiment match nearly perfectly up to instance ⑤, where the simulation slowly diverges from the experiment. Given that Krause (1979) reported that silica fiber stiffens under axial strain, we expected our linear-elastic model to slightly under predict the contact force, but the opposite occurred. The simulation reaches F = 0.631 N at $2b$ = 2.49 mm, which is 0.19 mm earlier than the experiment. If the polymer coatings deformed and allowed the fiber to nestle deeper into the faceplate grooves during the experiment the maximum possible adjustment to $2b$ would be $(0.245 - 0.140)/\cos 45^o$ = 0.15 mm. Thus, the polymer coating deformation may contribute to the discrepancy, but there must be other factors. Regardless, the difference is small. For the range of $2b$ values measured, the model does a reasonably good job of predicting the contact forces. By extension, it should be safe to assume that the model does an equally good job of predicting the stresses at the fiber apex.

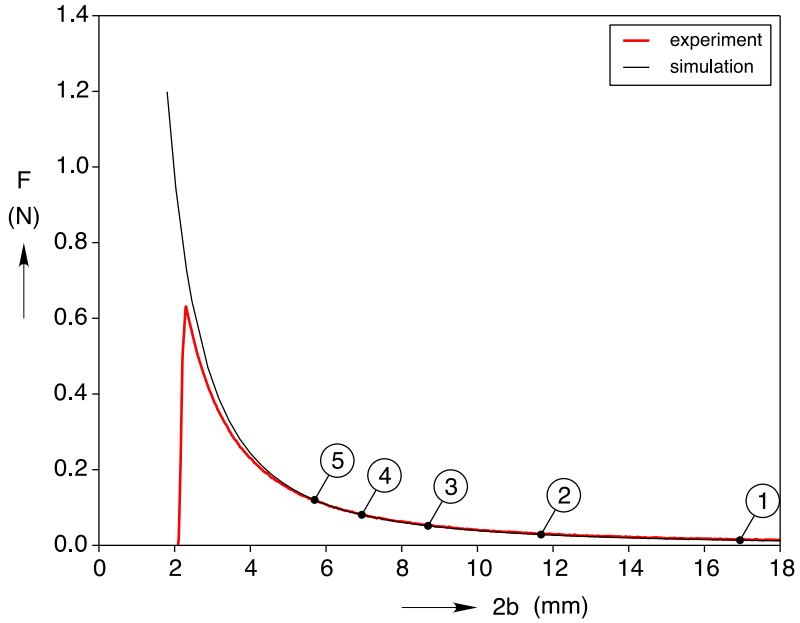

Figure 3-11. Comparison between the experimentally measured contact force and the predicted contact force.

The circled number instances correspond to the curves in Figure 3-9.

3.3 Future Modeling

If further resources were to be spent on model development and validation, we would recommend quantifying the effect of (1) the "Ω"- shape in Fig. 2 and (2) the silica stiffening.

The analysis in Section 2.2.1 utilizes Gulati's model (equivalent to Model A), which assumes that the fiber is bent into a "U"-shape. We have completed the important step of validating the model for this "U"-shape, but the auto-loader in the two-point bend tester causes the fiber to assume an "Ω"- shape. One could begin to investigate this using our beam FE model, but one would need to careful chose the boundary conditions to faithfully reproduce the effects of the auto-loader. If photos of the "Ω"- shape were collected and compared against, one could build confidence in simulations and determine whether the σ_a versus b is significantly different or not.

Stiffening of the silica material as tensile strain increases (Krause, 1979) could also affect the σ_a versus b curve. One might be tempted to simply take Equation 3-3 and input a modulus E that is a function of ε_a, but Equation 3-3 is predicated on the assumption of a linear elastic material. If the silica's response is significantly non-linear then the shape of the fiber would be different and Equation 3-2 would be invalid. On the other hand, it would be relatively straightforward to input a non-linear elastic model such as Mooney-Rivlin into our beam FE model and quickly assess the impact of the silica stiffening.

4 FIBER LIFE ESTIMATING

4.1 Fiber Life Estimating

4.1.1 Strength Degradation Mode and Experimental Determination of Material Parameters Needed for Lifetime Estimation

In fracture mechanics it is an accepted view that existing flaws or cracks are responsible for failure of brittle materials. Given a crack of length c and an applied stress σ_a, the stress intensity factor K_I is defined as:

$$K_1 = Y\sigma_a\sqrt{c}$$

Equation 4-1

The geometrical constant Y is determined by the shape of the crack. With the applied stress normal to the crack plane, failure occurs at $K_I = K_{Ic}$, the fracture toughness. At stress intensities $K_1 < K_{Ic}$ stress corrosion cracking can produce sub-critical crack growth. Given this crack growth, the crack length at failure c_f is longer than the initial length c. The initial crack length is estimated from experiments where the slow crack growth is minimized, for instance, in liquid nitrogen, vacuum, or in a dry atmosphere, or at high stress rate. The mechanism of sub-critical crack growth is well known in glasses, and in ceramics with glassy grain boundaries, and is shown schematically in Figure 4-1. .

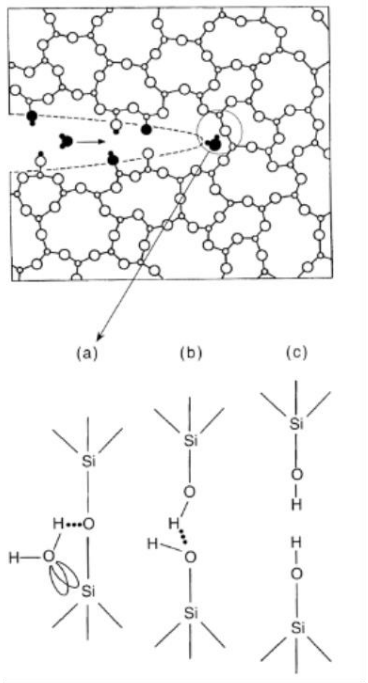

Figure 4-1. Schematic showing the mechanism for sub-critical crack growth in glasses

In the presence of stress and water, the following reaction is favored:

$$Si\text{-}0\text{-}\ Si + H_20 \rightarrow 2Si - OH$$

i.e., the Si-O bonds can break leading to crack extension. Under high stresses, bulk ceramics can fracture due to crack growth from this reaction. For high strength fiber optics, the initial crack length, c, is of the order of a few nm. Even growth of only a few nm can significantly bring down the high strength. In our application, the fibers will be exposed to a small level of bending strain while in assembly, and will be under this stress state in storage conditions (~50% RH) prior to launch. It is therefore essential that we quantify life due to this degradation mode and specify a certain safe design stress (equivalent to a safe bend radius). To accomplish this, we conducted two point bend testing on fibers at different stressing rates in a 50% RH environment. Two lots of the fiber were tested over a stressing rates range of 10^3. The results of these tests are shown in Figure 4-2.

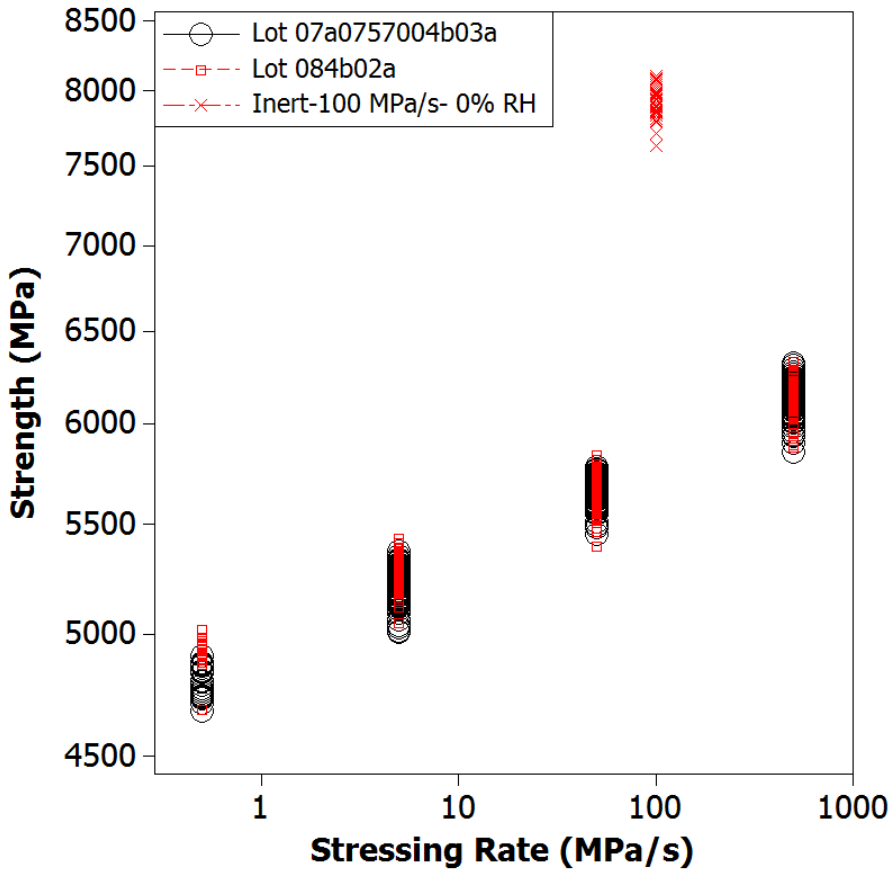

Figure 4-2. Strength as a function of stressing rate for fibers of interest.

It can be observed that the strength decreases as stressing rate decreases, a manifestation of the sub-critical crack growth phenomenon. Also plotted are inert strength values, obtained by testing at a fast rate, in very dry conditions.

If the crack velocity in the material in the sub-critical regime can be fitted to a power expression such as:

$$\text{Crack velocity, } v = \frac{dc}{dt} = A\left(\frac{K_1}{K_{1C}}\right)^n$$

Equation 4-2

then the strength as a function of stressing rate can be expressed by:

$$\log \sigma_f = \frac{1}{(n+1)} \log \dot{\sigma} + \log D$$

Equation 4-3

where σ_f is the fracture strength, and $\dot{\sigma}$ is the applied stressing rate. *D* is given by

$$D^{(n+1)} = \left(\frac{2K_{1c}{}^2 (n+1)}{AY^2 (n-2)}\right) S_i^{(n-2)}$$

Equation 4-4

where S_i is the inert strength of the material and Y (of order unity) is a geometrical factor dependent on the flaw shape, location, and orientation

Figure 4-3 shows the data fit to the form of Equation 4-3. From the slope of this curve, the value of the parameter n is obtained to 29, and that for D is 4775. This value, together with the known value of the fracture toughness of the materials, and the measured value of the inert strength was used to estimate the value of $A=3.66*10^{-6}$ m/s. With both n, and a known from our experiments, the crack velocity equation, Equation 4-2, is determined.

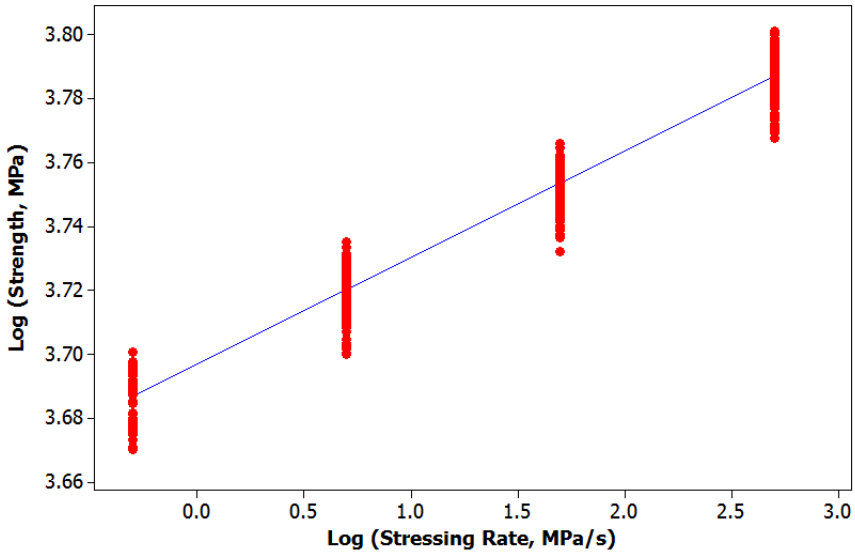

Figure 4-3. Log strength vs. log stressing rate

4.1.2 Predictive Model for Space Fiber Life Estimates

Differentiating Equation 4-1with respect to time, t, we obtain

$$\frac{\mathrm{dc}}{dt} = v = \frac{2K_I}{Y^2\sigma^2}\frac{dK_I}{dt} - \frac{2K_I^{\,2}}{Y^2\sigma^3}\frac{d\sigma}{dt}$$

Equation 4-5

If the fiber is under constant stress loading (as would be the case due to bending induced by putting the fiber in a geometrical configuration), $\sigma=\sigma_a$=constant. Hence,

$$dt = \frac{2K_I}{Y^2\sigma^2}\frac{dK_I}{v(K_I)}$$

Equation 4-6

Integrating Equation 4-6, we obtain the time to failure in this type of loading:

$$\int_0^{t_f} dt = t_f = \frac{2}{Y^2\sigma^2}\int_{K_{Ii}}^{K_{Ic}} \frac{K_I}{v(K_I)}dK_I$$

Equation 4-7

The time to failure is given by:

$$t_f {\sigma_a}^2 = \frac{2{K^2}_{Ic}}{AY^2(n-2)}\left(\frac{\sigma_a}{S_i}\right)^{2-n}$$

Equation 4-8

Value so K_{Ic}, Y, A, n, and S_i are all known from experiments and analysis, and the hence time to failure can easily be computed for our fiber for any applied stress. Equation 4-4 is a plot of the computed results. As expected, as the applied stress increases, the lifetime of the fiber, determined by the time for a crack to propagate critically through the fiber, goes down. Under conditions of storage in 50% Rh environment, a fiber under the stress of ~3000 MPa is expected to fracture in ~ 3.2 years (blue line on curve). Using bending formula, this corresponds to a bend radius of ~ 1.7 mm. Projected design radii are >20 times this number, and hence it can stated that strength loss of this fiber in storage environments will be negligible. The graph can also be used to compute a safe design stress, or a safe bend radius.

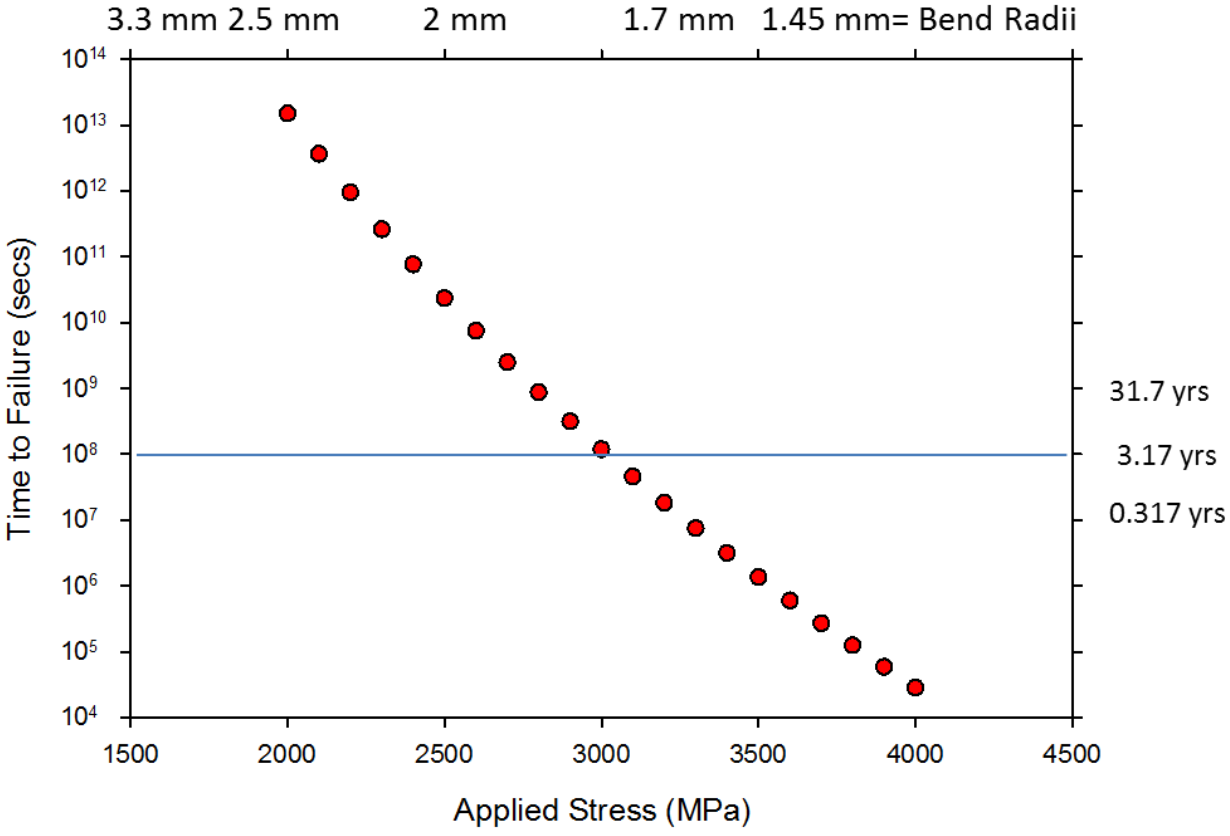

Figure 4-4. Computed lifetime results for fiber of interest based on the lifetime methodology enumerated in this section.

In order to test the accuracy of the predictions, fibers were wrapped around quartz high precision diameter mandrels, and exposed to a 50% Rh environment. Wrapping the fibers around the mandrels subjects their outer surface to a tensile stress, and the value of the strain can be calculated as glass diameter/(mandrel diameter+ overall fiber diameter). This strain can then be used to calculate the (constant) stress applied on the fiber due to the mandrel. In the experiment, mandrels of diameters 2.09, 2.22, 2.41, 2.42, 2.57, 2.6, 2.62, 2.77, 2.81, 3.19, and 3.2 mm were wrapped with ~ 1m length of fiber, and their fracture time monitored. For small diameter mandrels, failure occurred at short time interval and was monitored physically. For larger diameter mandrels (longer failure times), a set-up was constructed which passed light through the fiber. On fiber breakage, the light signal was interrupted, and the time to failure was automatically recorded. The time to failure (hrs.) for different mandrel sizes are shown in Figure 4-5. Each individual data point is depicted by an open red square. The predictions based on Equation 4-8 are shown as the black crosses.

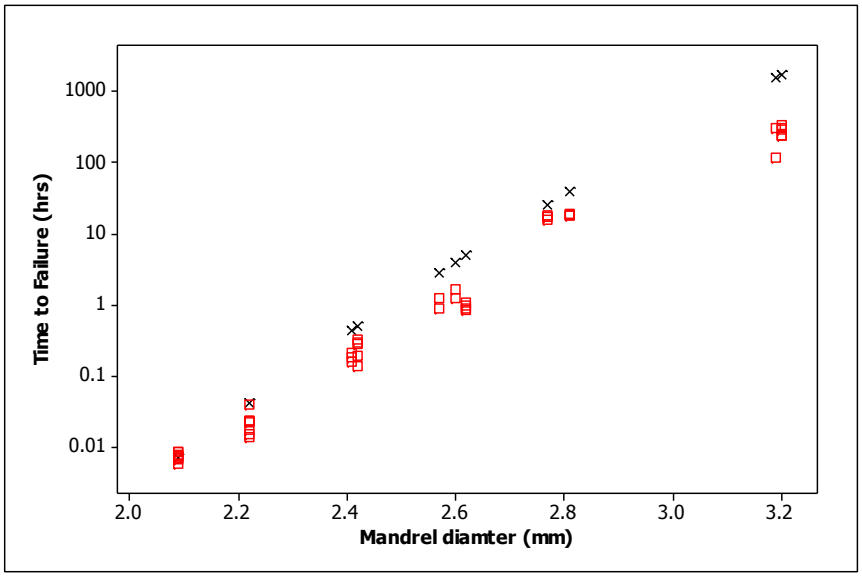

Figure 4-5. Comparison of predicted vs observed times to failure in mandrel wrap.

It can be observed that while the predictions closely track actual values for the short times, the two values begin to diverge for long periods, with the predictions being more optimistic. The reasons for the discrepancy could be that wrapping the fiber around the mandrel might be causing some handling damage that reduces the strength, or that the model is not adequate for lifetime prediction. In either case, these results serve as a caution. Additional work with mandrels of larger diameters leading to longer failure times is in progress. Nevertheless, the large safety factor in current designs would most likely preclude failure in the 3-year lifetime desired.

References

- "Space Flight Qualification on a Multifiber Ribbon Cable and Array Connector Assembly", X. L. Jin, M. N. Ott, F. V. LaRocca, R. M. Baker, B. E.N. Keeler, P. R. Friedberg, R. F. Chuska, M. C. Malenab, S. L. Macmurphy, 2005, Vol 6308, Proceedings – SPIE The International Society for Optical Engineering.

- "Development, qualification, and integration of the optical fiber array assemblies for the Lunar Reconnaissance Orbiter", M.N. Ott, R.. Switzer, R.. Chuska, F. LaRocca, W. J. Thomes, Jr., Shawn MacMurphy, SPIE Optics and Photonics Conference, Nanophotonics and Macrophotonics for Space Environments II, August 2008.

- "Fatigue of Materials," S. Suresh, Cambridge University Press, 1998

- "Stress-corrosion mechanisms in silicate glasses," Matteo Ciccotti, J. Phys. D: Appl. Phys. 42 (2009)

- "Subcritical Crack-Growth Behavior of Borosilicate Glass under Cyclic Loads: Evidence of a Mechanical Fatigue Effect," S. J. Dill, S. J. Bennison and R. H. Dauskardt, J. Am. Ceram. Soc., 80 [3] 773–76 (1997)6. "Mechanical Fatigue of Hybrid Glasses," M. S. Oliver and R. H. Dauskardt, Small 2010, 6, No. 17, 1892–18967. "Cyclic fatigue of high strength optical fibers in bending," M. J. Matthewson and V. Padiyar, SPIE Vol. 4215 (2001), pg. 53-59

- "Mechanical Fatigue of Hybrid Glasses," M. S. Oliver and R. H. Dauskardt, Small 2010, 6, No. 17, 1892-18967.

- "Cyclic fatigue of high strength optical fibers in bending," M. J. Matthewson and V. Padiyar, SPIE Vol. 4215 (2001), pg. 53-59.

- "Tensile fatigue properties of fibre Bragg grating optical fibre sensors", J. Ang, H.C.H. Li, I. Herszberg, M.K. Bannister, A.P. Mouritz, International Journal of Fatigue 32 (2010) 762–768.

- "Elastic property differences in a multi-mode optical fiber and the effect on predicted mechanical lifetime," R. Tandon, T. E. Buchheit, and D. M. Berry, Journal of Non-Crystalline Solids, v 358, n 6-7, p 1009-1013, April 1, 2012

- "Predicting Fracture in Micron-Scale Polycrystalline Silicon MEMS Structures," E. D. Reedy, Jr., B. L. Boyce, J. W. Foulk III, R. V. Field, Jr., M. P. de Boer, and S. S. Hazra, J. Microelectromech. Syst., 20 (2011), pp. 922-932.

- "Strength Measurement of Optical Fibers by Bending," M. J. Matthewson, C. R. Kurkjian, and S. T. Gulati, J. Am. Ceram. Soc., Vol. 69, No. 11 (1986), pp. 815-821

- Sierra Solid Mechanics Team. 2013. Sierra/Solid Mechanics VOTD User's Guide. Draft, March 21, 2013, pp. 227-233.

- "Deviations from linearity in the dependence of elongation upon force for fibers of simple glass formers and of glass optical lightguides", J. T. Krause, L. R. Testardi, and R. N. Thurston, Physics and Chemistry of Glasses, Vol. 20, No. 6 (1979), pp. 135-139

- "The elastica: a mathematical history", R. Levien, UCB/EECS-2008-103, Aug. 2008

- "Nonlinear Bending of Strong Glass Fibers", S.T. Gulati, for abstract see Am. Ceram. Soc. Bull., 60 [8] 862 (1981).

- "Matlab Documentation", Matlab R2013a, Mathworks, Natick, MA (2013)

- W.C. Oliver and G.M. Pharr (1992). An improved technique for determining hardness and elastic modulus using load and displacement sensing indentation experiments. Journal of Materials Research, 7, pp 1564-1583. doi:10.1557/JMR.1992.1564.

Distribution

1 Attn: John Matthewson
Department of Materials Science and Engineering
Rutgers University
607 Taylor Road
Piscataway, NJ 08854-8065

1	MS 0406	Ron Baker	5783 (electronic copy)
1	MS 0406	Todd Embree	5783 (electronic copy)
1	MS 0501	Mark Dowdican	5337 (electronic copy)
1	MS 0757	Kevin Brown	6625 (electronic copy)
1	MS 0840	Benjamin Reedlunn	1554 (electronic copy)
1	MS 0886	Garth Rohr	1835 (electronic copy)
1	MS 0888	Roger Rasberry	1835 (electronic copy)
1	MS 0889	Cory Gibson	1818 (electronic copy)
1	MS 0889	Raj Tandon	1818 (electronic copy)
1	MS 0973	Max Decker	5780 (electronic copy)
1	MS 1244	Jose Rodriquez	5532 (electronic copy)
1	MS 1244	Matt Napier	5555 (electronic copy)
1	MS 1244	Peter Stromberg	5556 (electronic copy)
1	MS 1244	Dave Godsey	5556 (electronic copy)
1	MS0359	D. Chavez, LDRD Office	7911 (electronic copy)
1	MS0899	Technical Library	9536 (electronic copy)


Sandia National Laboratories